Mathematical Models and Methods in Applied Sciences
Vol. 15, No. 12 (2005) 1863–1896

World Scientific
www.worldscientific.com

DYNAMICS OF THE GROUND STATE AND CENTRAL VORTEX STATES IN BOSE–EINSTEIN CONDENSATION

WEIZHU BAO* and YANZHI ZHANG†

Department of Computational Science,
National University of Singapore, Singapore 117543
**bao@cz3.nus.edu.sg*
†zhyanzhi@cz3.nus.edu.sg

Received 24 January 2004
Revised 11 January 2005
Communicated by P. Degond

In this paper, we study dynamics of the ground state and central vortex states in Bose–Einstein condensation (BEC) analytically and numerically. We show how to define the energy of the Thomas–Fermi (TF) approximation, prove that the ground state is a global minimizer of the energy functional over the unit sphere and all excited states are saddle points in linear case, derive a second-order ordinary differential equation (ODE) which shows that time-evolution of the condensate width is a periodic function with/without a perturbation by using the variance identity, prove that the angular momentum expectation is conserved in two dimensions (2D) with a radial symmetric trap and 3D with a cylindrical symmetric trap for any initial data, and study numerically stability of central vortex states as well as interaction between a few central vortices with winding numbers ± 1 by a fourth-order time-splitting sine-pseudospectral (TSSP) method. The merit of the numerical method is that it is explicit, unconditionally stable, time reversible and time transverse invariant. Moreover, it conserves the position density, performs spectral accuracy for spatial derivatives and fourth-order accuracy for time derivative, and possesses "optimal" spatial/temporal resolution in the semiclassical regime. Finally we find numerically the critical angular frequency for single vortex cycling from the ground state under a far-blue detuned Gaussian laser stirrer in strong repulsive interaction regime and compare our numerical results with those in the literatures.

Keywords: Bose–Einstein condensation; Gross–Pitaevskii equation; time-splitting sine-pseudospectral method; variance identity; ground state; central vortex state.

AMS Subject Classification: 81Q05, 65M70, 65N35, 65N25, 35B40

1. Introduction

Since its realization in dilute bosonic atomic gases,[2,14] Bose–Einstein condensation (BEC) of alkali atoms and hydrogen has been produced and studied extensively in the laboratory,[28] and has spurred great excitement in the atomic physics community and renewed the interest in studying the collective dynamics of macroscopic

ensembles of atoms occupying the same one-particle quantum state.[38,20] Theoretical predictions of the properties of a BEC like the density profile,[13] collective excitations[22] and the formation of vortices[42,1] can now be compared with experimental data.[2] Needless to say that this dramatic progress on the experimental front has stimulated a wave of activity on both theoretical and numerical aspects.

At temperature T much smaller than the critical temperature T_c,[32] a BEC is well described by the macroscopic wave function $\psi = \psi(\mathbf{x}, t)$ whose evolution is governed by a self-consistent, mean field nonlinear Schrödinger equation (NLSE) known as the Gross–Pitaevskii equation (GPE)[27,40]

$$i\hbar\partial_t\psi(\mathbf{x},t) = -\frac{\hbar^2}{2m}\nabla^2\psi(\mathbf{x},t) + V(\mathbf{x})\psi(\mathbf{x},t) + NU_0|\psi(\mathbf{x},t)|^2\psi(\mathbf{x},t), \tag{1.1}$$

where m is the atomic mass, $\hbar$ is the Planck constant, N is the number of atoms in the condensate, $V(\mathbf{x})$ is an external trapping potential. When a harmonic trap potential is considered, $V(\mathbf{x}) = \frac{m}{2}\left(\omega_x^2x^2 + \omega_y^2y^2 + \omega_z^2z^2\right)$ with ω_x, ω_y and ω_z being the trap frequencies in x-, y- and z-direction, respectively. $U_0 = 4\pi\hbar^2a_s/m$ describes the interaction between atoms in the condensate with a_s the s-wave scattering length. It is convenient to normalize the wave function by requiring

$$\|\psi(\cdot,t)\|^2 := \int_{\mathbb{R}^3}|\psi(\mathbf{x},t)|^2d\mathbf{x} = 1. \tag{1.2}$$

By introducing the dimensionless variables: $t \to t/\omega_m$ with $\omega_m = \min\{\omega_x, \omega_y, \omega_z\}$, $\mathbf{x} \to \mathbf{x}a_0$ with $a_0 = \sqrt{\frac{\hbar}{m\omega_m}}$, $\psi \to \psi/a_0^{3/2}$, we get the dimensionless GPE[12,6]

$$i\partial_t\psi(\mathbf{x},t) = -\frac{1}{2}\nabla^2\psi(\mathbf{x},t) + V(\mathbf{x})\psi(\mathbf{x},t) + \beta\,|\psi(\mathbf{x},t)|^2\psi(\mathbf{x},t), \tag{1.3}$$

where $\beta = \frac{U_0N}{a_0^3\hbar\omega_m} = \frac{4\pi a_sN}{a_0}$ and $V(\mathbf{x}) = \frac{1}{2}\left(\gamma_x^2x^2 + \gamma_y^2y^2 + \gamma_z^2z^2\right)$ with $\gamma_x = \frac{\omega_x}{\omega_m}$, $\gamma_y = \frac{\omega_y}{\omega_m}$ and $\gamma_z = \frac{\omega_z}{\omega_m}$. In the disk-shaped condensation, i.e. $\omega_x \approx \omega_y$ and $\omega_z \gg \omega_x$ ($\Leftrightarrow \gamma_x = 1$, $\gamma_y \approx 1$ and $\gamma_z \gg 1$ with $\omega_m = \omega_x$), the 3D GPE can be reduced to a 2D GPE.[33,12,6] Similarly, in a cigar-shaped condensation, i.e. $\omega_y \gg \omega_x$ and $\omega_z \gg \omega_x$ ($\Leftrightarrow \gamma_x = 1$, $\gamma_y \gg 1$ and $\gamma_z \gg 1$ with $\omega_m = \omega_x$), the 3D GPE can be reduced to a 1D GPE.[33,12,6] Thus here we consider the dimensionless GPE in d dimensions ($d = 1, 2, 3$):

$$i\partial_t\psi(\mathbf{x},t) = -\frac{1}{2}\nabla^2\psi + V_d(\mathbf{x})\psi + \beta_d\,|\psi|^2\psi, \quad \mathbf{x} \in \mathbb{R}^d, \tag{1.4}$$

$$\psi(\mathbf{x},0) = \psi_0(\mathbf{x}), \quad \mathbf{x} \in \mathbb{R}^d, \quad \text{with } \|\psi_0\|^2 := \int_{\mathbb{R}^d}|\psi_0(\mathbf{x})|^2d\mathbf{x} = 1, \tag{1.5}$$

with

$$\beta_d = \beta\begin{cases}\sqrt{\gamma_y\gamma_z}/2\pi, \\ \sqrt{\gamma_z/2\pi}, \\ 1,\end{cases} \qquad V_d(\mathbf{x}) = \begin{cases}\gamma_x^2x^2/2, & d = 1, \\ \left(\gamma_x^2x^2 + \gamma_y^2y^2\right)/2, & d = 2, \\ \left(\gamma_x^2x^2 + \gamma_y^2y^2 + \gamma_z^2z^2\right)/2, & d = 3,\end{cases} \tag{1.6}$$

where $\gamma_x > 0$, $\gamma_y > 0$ and $\gamma_z > 0$ are constants. Two important invariants of (1.4) are the *normalization of the wave function*

$$N(\psi) = \int_{\mathbb{R}^d} |\psi(\mathbf{x},t)|^2 d\mathbf{x} \equiv N(\psi_0) = \int_{\mathbb{R}^d} |\psi_0(\mathbf{x})|^2 \, d\mathbf{x} = 1, \quad t \geq 0 \tag{1.7}$$

and the *energy*

$$\begin{aligned} E_\beta(\psi) &= \int_{\mathbb{R}^d} \left[\frac{1}{2} |\nabla \psi(\mathbf{x},t)|^2 + V_d(\mathbf{x}) |\psi(\mathbf{x},t)|^2 + \frac{\beta_d}{2} |\psi(\mathbf{x},t)|^4 \right] d\mathbf{x} \\ &\equiv E_\beta(\psi_0), \quad t \geq 0. \end{aligned} \tag{1.8}$$

After BEC was achieved and observed in trapped neutral atomic vapors in 1995,[2,14] many theoretical and numerical studies have been done to understand it, e.g. theoretical study of BEC based on mean field theory[39,41,20,13,34] and kinetic model,[10,32,41] developing efficient and stable numerical method to compute ground state[43,19,4,12,16] and dynamics of BEC,[23,5,6,11,18] comparison with experiment results,[7] study of quantized vortex state[1,6,26,15,35,38,39,41,36,24,37] and multi-component BEC,[3,17,28] etc. Currently, there are still many open problems in the field, e.g. stability of stationary states, dynamics and interaction of quantized vortex, etc.

The aim of this paper is to study dynamics of the ground state and central vortex states in BEC analytically and numerically. In order to do so, we first prove that the ground state is a global minimizer of the energy functional over the unit sphere and all excited states are saddle points in linear GPE. Then we find a second-order ODE which governs the dynamics of condensate width. This ODE shows time-evolution of the condensate width is either a periodic function or a periodic function with a perturbation. The frequency of the periodic function is exactly double the trapping frequency in that direction. In fact, the frequency of the time-evolution of condensate width was obtained in physical literatures[23,43,18,6] based on either physical intuition or numerical results. Here we derive it in a mathematically rigorous way by using a second-order ODE. We also prove that the angular momentum expectation is conserved in 2D with a radial symmetric trap and 3D with a cylindrical symmetric trap under any initial data. Finally we study numerically the stability of central vortex states and their interaction by a fourth-order time-splitting sine-pseudospectral (TSSP4) method. This method is improved from the second-order time-splitting Fourier pseudo-spectral (TSFP2) method used in Refs. 3 and 6 for BEC in two aspects: (i) the Fourier basis is replaced by sine basis in spatial discretization due to the homogeneous Dirichlet boundary condition and thus the computational complexity per discrete transform is slightly smaller; (ii) the time-splitting scheme is improved from second-order to fourth-order and thus much larger time step can be chosen if very high accuracy is required. Therefore compared with previous methods in the literatures for BEC,[6] the new method can save computational time significantly. Our numerical results confirm the spectral order accuracy in space and fourth-order accuracy in time. The results show that

central vortices with winding number $m = \pm 1$ are dynamically stable, and respectively, unstable with $|m| > 1$, which agree with the results reported in the physical literatures.[15,29,30,37,42] But due to its high spatial/temporal resolution and other "good" properties, our new method works well when $\beta_d \gg 1$, i.e. in strong repulsive interaction regime, where the previous methods have difficulty in this regime.[15,26] Furthermore, we also apply the high spatial/temporal resolution method to study interaction between a few central vortices with winding numbers ± 1. Some interesting and complicated interaction patterns are observed from our numerical study.

The paper is organized as follows. In Sec. 2 we present stationary states including ground state and central vortex states. In Sec. 3 we study variation of stationary states in linear GPE, dynamics of condensate widths and conservation of angular momentum expectation mathematically. In Sec. 4 we present fourth/second-order time-splitting sine-pseudospectral method for GPE without/with external driven field respectively. In Sec. 5 we study dynamics of condensate widths, stability of central vortices and interaction of central vortex states numerically. In Sec. 6 some conclusions are drawn.

2. Stationary States

To find a stationary solution of (1.4), we write

$$\psi(\mathbf{x}, t) = e^{-i\mu t}\phi(\mathbf{x}), \tag{2.1}$$

where μ is the chemical potential of the condensate and ϕ is a function independent of time. Inserting (2.1) into (1.4) gives the following equation for $\phi(\mathbf{x})$

$$\mu\,\phi(\mathbf{x}) = -\frac{1}{2}\Delta\phi(\mathbf{x}) + V_d(\mathbf{x})\,\phi(\mathbf{x}) + \beta_d\,|\phi(\mathbf{x})|^2\phi(\mathbf{x}), \quad \mathbf{x} \in \mathbb{R}^d, \tag{2.2}$$

under the normalization condition

$$\|\phi\|^2 := \int_{\mathbb{R}^d} |\phi(\mathbf{x})|^2 d\mathbf{x} = 1. \tag{2.3}$$

This is a nonlinear eigenvalue problem under a constraint and any eigenvalue μ can be computed from its corresponding eigenfunction ϕ by

$$\begin{aligned}\mu = \mu_\beta(\phi) &= \int_{\mathbb{R}^d} \left[\frac{1}{2}\,|\nabla\phi(\mathbf{x})|^2 + V_d(\mathbf{x})\,|\phi(\mathbf{x})|^2 + \beta_d\,|\phi(\mathbf{x})|^4\right] d\mathbf{x} \\ &= E_\beta(\phi) + \int_{\mathbb{R}^d} \frac{\beta_d}{2}\,|\phi(\mathbf{x})|^4\,d\mathbf{x}.\end{aligned} \tag{2.4}$$

In fact, the eigenfunctions of (2.2) under the constraint (2.3) are equivalent to the critical points of the energy functional $E_\beta(\phi)$ over the unit sphere $S = \{\phi \mid \|\phi\| = 1, E_\beta(\phi) < \infty\}$. Furthermore, as noted in Ref. 4 they are also equivalent to the steady state solutions of the following continuous normalized gradient flow (CNGF):

$$\partial_t\phi = \frac{1}{2}\Delta\phi - V_d(\mathbf{x})\phi - \beta_d\,|\phi|^2\phi + \frac{\mu_\beta(\phi)}{\|\phi(\cdot,t)\|^2}\,\phi, \quad \mathbf{x} \in \mathbb{R}^d, \quad t \geq 0, \tag{2.5}$$

$$\phi(\mathbf{x}, 0) = \phi_0(\mathbf{x}), \qquad \mathbf{x} \in \mathbb{R}^d \text{ with } \|\phi_0\| = 1. \tag{2.6}$$

2.1. *Ground state*

The BEC ground state wave function $\phi_g(\mathbf{x})$ is found by minimizing the energy functional $E_\beta(\phi)$ over the unit sphere S: Find $(\mu_\beta^g, \phi_\beta^g \in S)$ such that

$$E_\beta^g = E_\beta(\phi_\beta^g) = \min_{\phi \in S} E_\beta(\phi), \quad \mu_\beta^g = \mu_\beta(\phi_\beta^g). \tag{2.7}$$

In the case of a defocusing condensate, i.e. $\beta_d \geq 0$, the energy functional $E_\beta(\phi)$ is positive, coercive and weakly lower semicontinuous on S, thus the existence of a minimum follows from the standard theory. To understand the uniqueness question, note that $E_\beta(\alpha\phi_\beta^g) = E_\beta(\phi_\beta^g)$ for all $\alpha \in \mathbb{C}$ with $|\alpha| = 1$. Thus an additional constraint has to be introduced to show uniqueness. For non-rotating BEC, the minimization problem (2.7) has a unique real valued non-negative ground state solution $\phi_\beta^g(\mathbf{x}) > 0$ for $\mathbf{x} \in \mathbb{R}^d$.[34]

When $\beta_d = 0$, the ground state solution is given explicitly[12]

$$\mu_0^g = \frac{1}{2}\begin{cases}\gamma_x, \\ \gamma_x + \gamma_y, \\ \gamma_x + \gamma_y + \gamma_z,\end{cases} \qquad \phi_0^g(\mathbf{x}) = \frac{1}{\pi^{d/4}}\begin{cases}\gamma_x^{1/4} e^{-\frac{\gamma_x x^2}{2}}, & d = 1, \\ (\gamma_x\gamma_y)^{1/4} e^{-\frac{\gamma_x x^2 + \gamma_y y^2}{2}}, & d = 2, \\ (\gamma_x\gamma_y\gamma_z)^{1/4} e^{-\frac{\gamma_x x^2 + \gamma_y y^2 + \gamma_z z^2}{2}}, & d = 3.\end{cases} \tag{2.8}$$

In fact, this solution can be viewed as an approximation of the ground state for weakly interacting condensate, i.e. $|\beta_d| \ll 1$. For a condensate with strong repulsive interaction, i.e. $\beta_d \gg 1$, $\gamma_x = O(1)$, $\gamma_y = O(1)$ and $\gamma_z = O(1)$ in (2.8), the ground state can be approximated by the TF approximation in this regime[12]:

$$\phi_\beta^{\mathrm{TF}}(\mathbf{x}) = \begin{cases}\sqrt{(\mu_\beta^{\mathrm{TF}} - V_d(\mathbf{x}))/\beta_d}, & V_d(\mathbf{x}) < \mu_\beta^{\mathrm{TF}}, \\ 0, & \text{otherwise},\end{cases} \tag{2.9}$$

$$\mu_\beta^{\mathrm{TF}} = \frac{1}{2}\begin{cases}(3\beta_1\gamma_x/2)^{2/3} & d = 1, \\ (4\beta_2\gamma_x\gamma_y/\pi)^{1/2} & d = 2, \\ (15\beta_3\gamma_x\gamma_y\gamma_z/4\pi)^{2/5} & d = 3.\end{cases} \tag{2.10}$$

As ϕ_β^{TF} is not differentiable at $V_d(\mathbf{x}) = \mu_\beta^{\mathrm{TF}}$, as noted in Refs. 12 and 6, $E_\beta(\phi_\beta^{\mathrm{TF}}) = \infty$ and $\mu_\beta(\phi_\beta^{\mathrm{TF}}) = \infty$. This shows that one cannot use (1.8) to define the energy of the TF approximation (2.9). How to define the energy of the TF approximation is not clear in the literatures. Using (2.4), (2.10) and (2.9), we present a way to define the energy of the TF approximation (2.9):

$$\begin{aligned} E_\beta^{\mathrm{TF}} \approx E_\beta(\phi_\beta^g) = \mu_\beta(\phi_\beta^g) - \int_{\mathbb{R}^d} \frac{\beta_d}{2}|\phi_\beta^{\mathrm{TF}}(\mathbf{x})|^4 d\mathbf{x} \approx \mu_\beta^{\mathrm{TF}} - \int_{\mathbb{R}^d} \frac{\beta_d}{2}|\phi_\beta^{\mathrm{TF}}(\mathbf{x})|^4 d\mathbf{x} \\ = \int_{\mathbb{R}^d}\left[V_d(\mathbf{x})|\phi_\beta^{\mathrm{TF}}(\mathbf{x})|^2 + \frac{\beta_d}{2}|\phi_\beta^{\mathrm{TF}}(\mathbf{x})|^4\right] d\mathbf{x} = \frac{d+2}{d+4}\,\mu_\beta^{\mathrm{TF}}, \quad d = 1, 2, 3. \end{aligned} \tag{2.11}$$

From the numerical results in Refs. 4 and 12, when $\gamma_x = O(1)$, $\gamma_y = O(1)$ and $\gamma_z = O(1)$, we can get

$$E_\beta^g - E_\beta^{\mathrm{TF}} = E_\beta(\phi_\beta^g) - E_\beta^{\mathrm{TF}} \to 0, \quad \text{as } \beta_d \to \infty.$$

Any eigenfunction $\phi(\mathbf{x})$ of (2.2) under constraint (2.3) whose energy $E_\beta(\phi) > E_\beta(\phi_\beta^g)$ is usually called as excited states in physical literatures.

2.2. *Central vortex states*

To find central vortex states in 2D with radial symmetry, i.e. $d = 2$ and $\gamma_x = \gamma_y = 1$ in (1.4), we write

$$\psi(\mathbf{x}, t) = e^{-i\mu_m t}\phi_m(x, y) = e^{-i\mu_m t}\phi_m(r)e^{im\theta}, \tag{2.12}$$

where (r, θ) is the polar coordinate, $m \neq 0$ is an integer and is called as index or winding number, μ_m is the chemical potential, and $\phi_m(r)$ is a real function independent of time. Inserting (2.12) into (1.4) gives the following equation for $\phi_m(r)$

$$\mu_m\phi_m(r) = \left[-\frac{1}{2r}\frac{d}{dr}\left(r\frac{d}{dr}\right) + \frac{1}{2}\left(r^2 + \frac{m^2}{r^2}\right) + \beta_2|\phi_m|^2\right]\phi_m, \quad 0 < r < \infty, \tag{2.13}$$

$$\phi_m(0) = 0, \quad \lim_{r\to\infty}\phi_m(r) = 0, \tag{2.14}$$

under the normalization condition

$$2\pi\int_0^\infty |\phi_m(r)|^2\, r\, dr = 1. \tag{2.15}$$

In order to find the central vortex state $\phi_\beta^m(x, y) = \phi_\beta^m(r)e^{im\theta}$ with index m, we find a real non-negative function $\phi_\beta^m(r)$ which minimizes the energy functional

$$\begin{aligned} E_\beta^m(\phi(r)) &= E_\beta(\phi(r)e^{im\theta}) \\ &= \pi\int_0^\infty \left[|\phi'(r)|^2 + \left(r^2 + \frac{m^2}{r^2}\right)|\phi(r)|^2 + \beta_2|\phi(r)|^4\right] r dr, \end{aligned} \tag{2.16}$$

over the set $S_0 = \{\phi | 2\pi\int_0^\infty |\phi(r)|^2 r\ dr = 1, \phi(0) = 0, E_\beta^m(\phi) < \infty\}$. The existence and uniqueness of non-negative minimizer for this minimization problem can be obtained similarly as for the ground state.[34] Note that the set $S_m = \{\phi(r)e^{im\theta} \mid \phi \in S_0\} \subset S$ is a subset of the unit sphere, so $\phi_\beta^m(r)e^{im\theta}$ is a minimizer of the energy functional $E_\beta(\phi)$ over the set $S_m \subset S$. When $\beta_2 = 0$ in (1.4), $\phi_0^m(r) = \frac{1}{\sqrt{\pi|m|!}} r^{|m|}e^{-r^2/2}$.[4]

Similarly, in order to find central vortex line states in 3D with cylindrical symmetry, i.e. $d = 3$ and $\gamma_x = \gamma_y = 1$ in (1.4), we write

$$\psi(\mathbf{x}, t) = e^{-i\mu_m t}\phi_m(x, y, z) = e^{-i\mu_m t}\phi_m(r, z)e^{im\theta}, \tag{2.17}$$

where $m \neq 0$ is an integer and is called an index, μ_m is the chemical potential and $\phi_m(r, z)$ is a real function independent of time. Inserting (2.17) into (1.4) with

$d = 3$ gives the following equation for $\phi_m(r, z)$

$$\mu_m \phi_m = \left[-\frac{1}{2r}\frac{\partial}{\partial r}\left(r\frac{\partial}{\partial r}\right) - \frac{\partial^2}{2\,\partial z^2} + \frac{1}{2}\left(r^2 + \frac{m^2}{r^2} + \gamma_z^2 z^2\right) + \beta\,|\phi_m|^2\right]\phi_m, \quad (2.18)$$

$$\phi_m(0, z) = 0, \quad \lim_{r\to\infty} \phi_m(r, z) = 0, \quad -\infty < z < \infty, \quad (2.19)$$

$$\lim_{|z|\to\infty} \phi_m(r, z) = 0, \quad 0 \le r < \infty, \quad (2.20)$$

under the normalization condition

$$2\pi \int_0^\infty \int_{-\infty}^\infty |\phi_m(r, z)|^2 r\, dr\, dz = 1. \quad (2.21)$$

In order to find the central vortex line state $\phi_\beta^m(x, y, z) = \phi_\beta^m(r, z)e^{im\theta}$ with index m, we find a real non-negative function $\phi_\beta^m(r, z)$ which minimizes the energy functional

$$\begin{aligned} E_\beta^m(\phi(r, z)) &= E_\beta(\phi(r, z)e^{im\theta}) \\ &= \pi \int_0^\infty \int_{-\infty}^\infty \left[|\phi_r|^2 + |\phi_z|^2 + \left(r^2 + \gamma_z^2 z^2 + \frac{m^2}{r^2}\right)|\phi|^2 + \beta|\phi|^4\right] r\, dr\, dz, \end{aligned} \quad (2.22)$$

over the set $S_0 = \{\phi | 2\pi \int_0^\infty \int_{-\infty}^\infty |\phi(r, z)|^2 r dr\, dz = 1, \phi(0, z) = 0, -\infty < z < \infty, E_\beta^m(\phi) < \infty\}$. The existence and uniqueness of non-negative minimizer for this minimization problem can be obtained similarly as for the ground state.[34] Note that the set $S_m = \{\phi(r, z)e^{im\theta} \mid \phi \in S_0\} \subset S$ is a subset of the unit sphere, so $\phi_\beta^m(r, z)e^{im\theta}$ is a minimizer of the energy functional $E_\beta(\phi)$ over the set S_m. When $\beta = 0$ in (1.4), $\phi_0^m(r, z) = \frac{\gamma_z^{1/4}}{\pi^{3/4}\sqrt{|m|!}} r^{|m|} e^{-(r^2+\gamma_z z^2)/2}$.[4]

3. Dynamics of the Stationary States

In this section, we first prove that the ground state is a global minimizer of the energy functional (1.8) over the unit sphere and all excited states are saddle points in linear GPE. Then we find a second-order ODE which governs the dynamics of condensate widths. Finally we show that the angular momentum expectation is conserved in 2D and 3D with a symmetric trap under any initial data.

3.1. *Variation of stationary states over the unit sphere*

For the stationary states of (2.2), we have the following lemma:

Lemma 3.1. *Suppose $\beta_d = 0$ and $V_d(\mathbf{x}) \ge 0$ for $\mathbf{x} \in \mathbb{R}^d$, we have*

(i) *The ground state ϕ_g is a global minimizer of $E_0(\phi)$ over S.*
(ii) *Any excited state ϕ_j is a saddle point of $E_0(\phi)$ over S.*

Proof. Let ϕ_e be an eigenfunction of the eigenvalue problem (2.2) and (2.3). The corresponding eigenvalue is μ_e. For any function ϕ such that $E_0(\phi) < \infty$ and $\|\phi_e + \phi\| = 1$, note that (2.3), we have

$$\begin{aligned}\|\phi\|^2 &= \|\phi + \phi_e\|^2 - \|\phi_e\|^2 - \int_{\mathbb{R}^d} (\phi^* \phi_e + \phi \phi_e^*) d\mathbf{x} \\ &= -\int_{\mathbb{R}^d} (\phi^* \phi_e + \phi \phi_e^*) d\mathbf{x}. \end{aligned} \tag{3.1}$$

From (1.8) with $\psi = \phi_e + \phi$, note that (2.3) and (3.1), integration by parts, we get

$$\begin{aligned} E_0(\phi_e + \phi) &= \int_{\mathbb{R}^d} \left[\frac{1}{2}|\nabla \phi_e + \nabla \phi|^2 + V_d(\mathbf{x})|\phi_e + \phi|^2\right] d\mathbf{x} \\ &= \int_{\mathbb{R}^d} \left[\frac{1}{2}|\nabla \phi_e|^2 + V_d(\mathbf{x})|\phi_e|^2\right] d\mathbf{x} + \int_{\mathbb{R}^d} \left[\frac{1}{2}|\nabla \phi|^2 + V_d(\mathbf{x})|\phi|^2\right] d\mathbf{x} \\ &\quad + \int_{\mathbb{R}^d} \left[\left(-\frac{1}{2}\Delta \phi_e + V_d(\mathbf{x})\phi_e\right)^* \phi + \left(-\frac{1}{2}\Delta \phi_e + V_d(\mathbf{x})\phi_e\right) \phi^*\right] d\mathbf{x} \\ &= E_0(\phi_e) + E_0(\phi) + \int_{\mathbb{R}^d} (\mu_e\, \phi_e^*\, \phi + \mu_e\, \phi_e\, \phi^*) d\mathbf{x} \\ &= E_0(\phi_e) + E_0(\phi) - \mu_e \|\phi\|^2 = E_0(\phi_e) + [E_0(\phi/\|\phi\|) - \mu_e]\, \|\phi\|^2. \end{aligned} \tag{3.2}$$

(i) Taking $\phi_e = \phi_g$ and $\mu_e = \mu_g$ in (3.2) and noticing $E_0(\phi/\|\phi\|) \geq E_0(\phi_g) = \mu_g$ for any $\phi \neq 0$, we get immediately that ϕ_g is a global minimizer of $E_0(\phi)$ over S.

(ii) Taking $\phi_e = \phi_j$ and $\mu_e = \mu_j$ in (3.2), since $E_0(\phi_g) < E_0(\phi_j)$ and it is easy to find an eigenfunction ϕ of (2.2) such that $E_0(\phi) > E_0(\phi_j)$, we get immediately that ϕ_j is a saddle point of the functional $E_0(\phi)$ over S. □

3.2. *Dynamics of condensate widths*

To quantify the dynamics of problems (1.4), (1.5), we define the condensate widths along the α-axis ($\alpha = x, y, z$) as

$$\delta_\alpha(t) = \langle \alpha^2 \rangle(t) = \int_{\mathbb{R}^d} \alpha^2 |\psi(\mathbf{x}, t)|^2\, d\mathbf{x}, \quad \sigma_\alpha(t) = \sqrt{\delta_\alpha(t)}. \tag{3.3}$$

Lemma 3.2. *Suppose $\psi(\mathbf{x}, t)$ is the solution of problems* (1.4), (1.5), *then we have*

$$\frac{d^2 \delta_\alpha(t)}{dt^2} = -2\gamma_\alpha^2 \delta_\alpha(t) + \int_{\mathbb{R}^d} \left(2|\partial_\alpha \psi|^2 + \beta_d |\psi|^4\right) d\mathbf{x}, \quad t \geq 0, \tag{3.4}$$

$$\delta_\alpha(0) = \delta_\alpha^{(0)} = \int_{\mathbb{R}^d} \alpha^2 |\psi_0(\mathbf{x})|^2\, d\mathbf{x}, \quad \alpha = x, y, z, \tag{3.5}$$

$$\delta_\alpha'(0) = \delta_\alpha^{(1)} = \mathrm{Im}\left[\int_{\mathbb{R}^d} \alpha\, (\psi_0^*\, \partial_\alpha \psi_0 - \psi_0\, \partial_\alpha \psi_0^*)\, d\mathbf{x}\right], \tag{3.6}$$

where f^* and $\mathrm{Im}(f)$ denote the conjugate and imaginary part of f respectively.

Proof. Differentiate (3.3) with respect to t, notice (1.4), integrate by parts, we have

$$\begin{aligned}\frac{d\delta_\alpha(t)}{dt} &= \frac{d}{dt}\int_{\mathbb{R}^d}\alpha^2|\psi(\mathbf{x},t)|^2\,d\mathbf{x} = \int_{\mathbb{R}^d}\alpha^2\,(\psi\,\partial_t\psi^* + \psi^*\,\partial_t\psi)d\mathbf{x}\\ &= \frac{i}{2}\int_{\mathbb{R}^d}\alpha^2\,(\psi^*\Delta\psi - \psi\Delta\psi^*)d\mathbf{x} = i\int_{\mathbb{R}^d}\alpha\,(\psi\,\partial_\alpha\psi^* - \psi^*\,\partial_\alpha\psi)d\mathbf{x}. \qquad (3.7)\end{aligned}$$

Similarly, differentiate (3.7) with respect to t, notice (1.4), integrate by parts, we have

$$\begin{aligned}\frac{d^2\delta_\alpha(t)}{dt^2} &= i\int_{\mathbb{R}^d}\alpha\,[\partial_t\psi\,\partial_\alpha\psi^* + \psi\,\partial_{\alpha\,t}\psi^* - \partial_t\psi^*\,\partial_\alpha\psi - \psi^*\,\partial_{\alpha\,t}\psi]d\mathbf{x}\\ &= \int_{\mathbb{R}^d}[2i\alpha\,(\partial_t\psi\,\partial_\alpha\psi^* - \partial_t\psi^*\,\partial_\alpha\psi) + i\,(\psi^*\,\partial_t\psi - \psi\,\partial_t\psi^*)]\,d\mathbf{x}\\ &= \int_{\mathbb{R}^d}\Big[-\alpha\,(\partial_\alpha\psi^*\,\Delta\psi + \partial_\alpha\psi\,\Delta\psi^*) + 2\alpha V_d(\mathbf{x})\,(\psi\,\partial_\alpha\psi^* + \psi^*\,\partial_\alpha\psi)\\ &\quad - \frac{1}{2}\,(\psi^*\,\Delta\psi + \psi\,\Delta\psi^*) + 2\beta_d\alpha|\psi|^2\,(\psi\,\partial_\alpha\psi^* + \psi^*\,\partial_\alpha\psi)\\ &\quad + 2V_d(\mathbf{x})|\psi|^2 + 2\beta_d|\psi|^4\Big]d\mathbf{x}\\ &= \int_{\mathbb{R}^d}\Big[2|\partial_\alpha\psi|^2 - |\nabla\psi|^2 - |\psi|^2\partial_\alpha\,(2\alpha V_d(\mathbf{x})) - \beta_d|\psi|^4 + |\nabla\psi|^2\\ &\quad + 2V_d(\mathbf{x})|\psi|^2 + 2\beta_d|\psi|^4\Big]\,d\mathbf{x}\\ &= \int_{\mathbb{R}^d}\left[2|\partial_\alpha\psi|^2 + \beta_d|\psi|^4 - 2\alpha|\psi|^2\,\partial_\alpha(V_d(\mathbf{x}))\right]d\mathbf{x}. \qquad (3.8)\end{aligned}$$

Thus the desired equality (3.4) is a combination of (3.3), (3.8) and (1.6). □

Lemma 3.3. (i) *In 1D without interaction, i.e. $d = 1$ and $\beta_d = 0$ in (1.4), we have*

$$\delta_x(t) = \frac{E_0(\psi_0)}{\gamma_x^2} + \left(\delta_x^{(0)} - \frac{E_0(\psi_0)}{\gamma_x^2}\right)\cos(2\gamma_x t) + \frac{\delta_x^{(1)}}{2\gamma_x}\sin(2\gamma_x t), \quad t \geq 0. \qquad (3.9)$$

(ii) *In 2D with a radial symmetric trap, i.e. $d = 2$ and $\gamma_x = \gamma_y := \gamma_r$ in (1.4), for any initial data $\psi_0(x, y)$ in (1.5), we have*

$$\delta_r(t) = \frac{E_\beta(\psi_0)}{\gamma_r^2} + \left(\delta_r^{(0)} - \frac{E_\beta(\psi_0)}{\gamma_r^2}\right)\cos(2\gamma_r t) + \frac{\delta_r^{(1)}}{2\gamma_r}\sin(2\gamma_r t), \quad t \geq 0, \qquad (3.10)$$

where

$$\delta_r(t) = \delta_x(t) + \delta_y(t), \quad \delta_r^{(0)} := \delta_r(0) = \delta_x(0) + \delta_y(0), \quad \delta_r^{(1)} := \delta_r'(0) = \delta_x'(0) + \delta_y'(0).$$

Furthermore, when $d = 2$ and $\gamma_x = \gamma_y$ in (1.4) and the initial data $\psi_0(\mathbf{x})$ in (1.5) satisfying

$$\psi_0(x, y) = f(r)e^{im\theta} \quad \textit{with } m \in \mathbb{Z} \quad \textit{and} \quad f(0) = 0 \textit{ when } m \neq 0, \qquad (3.11)$$

we have

$$\delta_x(t) = \delta_y(t) = \frac{1}{2}\delta_r(t)$$
$$= \frac{E_\beta(\psi_0)}{2\gamma_x^2} + \left(\delta_x^{(0)} - \frac{E_\beta(\psi_0)}{2\gamma_x^2}\right)\cos(2\gamma_x t) + \frac{\delta_x^{(1)}}{2\gamma_x}\sin(2\gamma_x t), \quad t \geq 0. \tag{3.12}$$

(iii) *For all other cases, we have*

$$\delta_\alpha(t) = \frac{E_\beta(\psi_0)}{\gamma_\alpha^2} + \left(\delta_\alpha^{(0)} - \frac{E_\beta(\psi_0)}{\gamma_\alpha^2}\right)\cos(2\gamma_\alpha t) + \frac{\delta_\alpha^{(1)}}{2\gamma_\alpha}\sin(2\gamma_\alpha t) + g_\alpha(t), \quad t \geq 0, \tag{3.13}$$

where $g_\alpha(t)$ is a solution of the following problem

$$\frac{d^2 g_\alpha(t)}{dt^2} + 4\gamma_\alpha^2 g_\alpha(t) = f_\alpha(t), \quad g_\alpha(0) = \frac{dg_\alpha(0)}{dt} = 0, \tag{3.14}$$

with

$$f_\alpha(t) = \int_{\mathbb{R}^d} \left[2|\partial_\alpha \psi|^2 - 2|\nabla\psi|^2 - \beta_d|\psi|^4 + (2\gamma_\alpha^2\alpha^2 - 4V_d(\mathbf{x}))|\psi|^2\right] d\mathbf{x}$$

satisfying

$$|f_\alpha(t)| < 4E_\beta(\psi_0), \quad t \geq 0.$$

Proof. (i) From (3.4) with $d = 1$ and $\beta_1 = 0$ and from (1.8), we have

$$\frac{d^2\delta_x(t)}{dt^2} = 4E_0(\psi_0) - 4\gamma_x^2\delta_x(t), \quad t > 0, \tag{3.15}$$
$$\delta_x(0) = \delta_x^{(0)}, \quad \delta_x'(0) = \delta_x^{(1)}. \tag{3.16}$$

Thus (3.9) is the unique solution of the second-order ODE (3.15) with the initial data (3.16).

(ii) From (3.4) with $d = 2$, we have

$$\frac{d^2\delta_x(t)}{dt^2} = -2\gamma_x^2\delta_x(t) + \int_{\mathbb{R}^d}\left(2|\partial_x\psi|^2 + \beta_2|\psi|^4\right)d\mathbf{x}, \tag{3.17}$$
$$\frac{d^2\delta_y(t)}{dt^2} = -2\gamma_y^2\delta_y(t) + \int_{\mathbb{R}^d}\left(2|\partial_y\psi|^2 + \beta_2|\psi|^4\right)d\mathbf{x}. \tag{3.18}$$

Add (3.17) and (3.18) with (1.8) and $\gamma_x = \gamma_y$, we have the ODE for $\delta_r(t)$:

$$\frac{d^2\delta_r(t)}{dt^2} = 4E_\beta(\psi_0) - 4\gamma_r^2\delta_r(t), \quad t > 0, \tag{3.19}$$
$$\delta_r(0) = \delta_r^{(0)}, \quad \delta_r'(0) = \delta_r^{(1)}. \tag{3.20}$$

Thus (3.10) is the unique solution of the second-order ODE (3.19) with the initial data (3.20). Furthermore, when the initial data $\psi_0(\mathbf{x})$ in (1.5) satisfies (3.11), due to the radial symmetry, the solution $\psi(\mathbf{x}, t)$ of (1.4)–(1.5) satisfies

$$\psi(x, y, t) = g(r, t)e^{im\theta} \quad \text{with } g(r, 0) = f(r). \tag{3.21}$$

This implies

$$\begin{aligned}\delta_x(t) &= \int_{\mathbb{R}^2} x^2 |\psi(x, y, t)|^2 d\mathbf{x} = \int_0^\infty \int_0^{2\pi} r^2 \cos^2\theta \, |g(r, t)|^2 r \, d\theta \, dr \\ &= \pi \int_0^\infty r^2 |g(r, t)|^2 r \, dr = \int_0^\infty \int_0^{2\pi} r^2 \sin^2\theta \, |g(r, t)|^2 r \, d\theta \, dr \\ &= \int_{\mathbb{R}^2} y^2 |\psi(x, y, t)|^2 d\mathbf{x} = \delta_y(t), \quad t \geq 0. \end{aligned} \tag{3.22}$$

Thus the equality (3.12) is a combination of (3.22) and (3.10).

(iii) From (3.4), notice the energy conservation (1.8) of the GPE (1.4), we have

$$\frac{d^2\delta_\alpha(t)}{dt^2} = 4E_\beta(\psi_0) - 4\gamma_\alpha^2 \delta_\alpha(t) + f_\alpha(t), \quad t \geq 0. \tag{3.23}$$

Thus (3.13) is the unique solution of the second-order ODE (3.23) with the initial data (3.5), (3.6). □

3.3. *Conservation of angular momentum expectation*

Another important quantity for studying dynamics of BEC in 2D and 3D, especially for measuring the appearance of vortex, is the angular momentum expectation value defined as

$$\langle L_z \rangle(t) := \int_{\mathbb{R}^d} \psi^*(\mathbf{x}, t) L_z \psi(\mathbf{x}, t) d\mathbf{x}, \quad t \geq 0, \quad d = 2, 3, \tag{3.24}$$

where $L_z = i\,(y\partial_x - x\partial_y)$ is the z-component angular momentum.

Lemma 3.4. *Suppose $\psi(\mathbf{x}, t)$ is the solution of problems* (1.4), (1.5) *with $d = 2$ or* 3, *then we have*

$$\frac{d\langle L_z \rangle(t)}{dt} = \left(\gamma_x^2 - \gamma_y^2\right) \delta_{xy}(t), \quad \delta_{xy}(t) = \int_{\mathbb{R}^d} xy |\psi(\mathbf{x}, t)|^2 d\mathbf{x}, \quad t \geq 0. \tag{3.25}$$

This implies that, at least in the following two cases, the angular momentum expectation is conserved:

(i) *For any given initial data $\psi_0(\mathbf{x})$ in* (1.5), *if the trap is radial symmetric in 2D, and resp., cylindrical symmetric in 3D, i.e. $\gamma_x = \gamma_y$;*

(ii) *For any given $\gamma_x > 0$ and $\gamma_y > 0$ in* (1.6), *if the initial data $\psi_0(\mathbf{x})$ in* (1.5) *is even in the first variable x or second variable y.*

Proof. Differentiate (3.24) with respect to t, (1.4), integrate by parts, we have

$$\begin{aligned}
\frac{d\langle L_z\rangle(t)}{dt} &= \int_{\mathbb{R}^d} [(i\psi_t^*)\,(y\partial_x - x\partial_y)\psi + \psi^*(y\partial_x - x\partial_y)(i\psi_t)]d\mathbf{x} \\
&= \int_{\mathbb{R}^d} \left[\left(\frac{1}{2}\nabla^2\psi^* - V_d(\mathbf{x})\psi^* - \beta_d|\psi|^2\psi^*\right)(y\partial_x - x\partial_y)\psi\right. \\
&\quad \left. + \psi^*(y\partial_x - x\partial_y)\left(-\frac{1}{2}\nabla^2\psi + V_d(\mathbf{x})\psi + \beta_d|\psi|^2\psi\right)\right]d\mathbf{x} \\
&= \int_{\mathbb{R}^d} \frac{1}{2}\left[\nabla^2\psi^*(y\partial_x - x\partial_y)\psi - \psi^*(y\partial_x - x\partial_y)\nabla^2\psi\right]d\mathbf{x} \\
&\quad + \int_{\mathbb{R}^d} \left[\psi^*(y\partial_x - x\partial_y)\left(V_d(\mathbf{x})\psi + \beta_d|\psi|^2\psi\right)\right. \\
&\quad \left. - \left(V_d(\mathbf{x})\psi^* + \beta_d|\psi|^2\psi^*\right)\,(y\partial_x - x\partial_y)\psi\right]d\mathbf{x} \\
&= \int_{\mathbb{R}^d} |\psi|^2(y\partial_x - x\partial_y)\left(V_d(\mathbf{x}) + \beta_d|\psi|^2\right)d\mathbf{x} \\
&= \int_{\mathbb{R}^d} |\psi|^2(y\partial_x - x\partial_y)V_d(\mathbf{x})d\mathbf{x} = \int_{\mathbb{R}^d} |\psi|^2(\gamma_x^2 - \gamma_y^2)xy\,d\mathbf{x} \\
&= (\gamma_x^2 - \gamma_y^2)\int_{\mathbb{R}^d} xy|\psi|^2\,d\mathbf{x}, \quad t \geq 0. \qquad (3.26)
\end{aligned}$$

For case (i), since $\gamma_x = \gamma_y$, we get the conservation of $\langle L_z\rangle$ immediately from the first-order ODE:

$$\frac{d\langle L_z\rangle(t)}{dt} = 0, \quad t \geq 0. \qquad (3.27)$$

For case (ii), we know that the solution $\psi(\mathbf{x}, t)$ is even in the first variable x or second variable y due to the assumption of the initial data and symmetry of $V_d(\mathbf{x})$. Thus $|\psi(\mathbf{x}, t)|$ is even in either x or y, which immediately implies that $\langle L_z\rangle$ satisfies the first-order ODE (3.27). □

4. Time-Splitting Sine Pseudospectral (TSSP) Method

In this section we present time-splitting sine pseudospectral (TSSP) methods for the problems (1.4), (1.5) with/without external driven field with homogeneous Dirichlet boundary conditions. For simplicity of notation we shall introduce the method for the case of one space dimension ($d = 1$). Generalizations to $d > 1$ are straightforward for tensor product grids and the results remain valid without modifications. For $d = 1$, the problem with an external driven field becomes

$$i\partial_t\psi = -\frac{1}{2}\partial_{xx}\psi + V_1(x)\psi + W(x,t)\psi + \beta_1|\psi|^2\psi, \quad a < x < b, \quad t > 0, \qquad (4.1)$$

$$\psi(x, t = 0) = \psi_0(x), \quad a \leq x \leq b, \quad \psi(a,t) = \psi(b,t) = 0, \quad t \geq 0; \qquad (4.2)$$

where $W(x,t)$ is an external driven field. Typical external driven fields used in physical literatures include a far-blued detuned Gaussian laser beam stirrer[15]

$$W(\mathbf{x},t) = W_s(t)\exp\left[-\left(\frac{|\mathbf{x}-\mathbf{x}_s(t)|^2}{w_s/2}\right)\right], \tag{4.3}$$

with W_s the height, w_s the width, and $\mathbf{x}_s(t)$ the position of the stirrer; or a Delta-kicked potential[31]

$$W(x,t) = K\cos(kx)\sum_{n=-\infty}^{\infty}\delta(t-n\tau), \tag{4.4}$$

with K the kick strength, k the wave number, τ the time interval between kicks, and $\delta(\tau)$ is the Dirac delta function. In order to present the TSSP method, we rewrite (4.1) in the form

$$i\,\partial_t\psi = A\,\psi + B\,\psi, \tag{4.5}$$

where A and B are two operators and they do not need to commute.

We choose the spatial mesh size $h = \Delta x > 0$ with $h = (b-a)/M$ for M an even positive integer, and let $x_j := a + j\,h$, $j = 0, 1, \ldots, M$. Let ψ_j^n be the approximation of $\psi(x_j, t_n)$ and ψ^n be the solution vector at time $t = t_n = nk$ with components ψ_j^n.

4.1. *Fourth-order TSSP for GPE without external driven field*

When $W(x,t) \equiv 0$, i.e. without external driven field, the GPE (4.1) can be written in the form of (4.5) with

$$A\psi = V_1(x)\psi(x,t) + \beta_1|\psi(x,t)|^2\psi(x,t), \quad B\psi = -\frac{1}{2}\partial_{xx}\psi(x,t). \tag{4.6}$$

Thus, the key for an efficient implementation of time-splitting is to solve efficiently the following two subproblems:

$$i\,\partial_t\psi(x,t) = B\psi = -\frac{1}{2}\partial_{xx}\psi \tag{4.7}$$

and

$$i\,\partial_t\psi(x,t) = A\,\psi = V_1(x)\psi(x,t) + \beta_1|\psi(x,t)|^2\psi(x,t). \tag{4.8}$$

Equation (4.7) will be discretized in space by the sine pseudospectral method and integrated in time *exactly*. For $t \in [t_n, t_{n+1}]$, the ODE (4.8) leaves $|\psi|$ invariant in[9,8] t and therefore becomes

$$i\psi_t(x,t) = V_1(x)\psi(x,t) + \beta_1|\psi(x,t_n)|^2\psi(x,t) \tag{4.9}$$

and thus can be integrated *exactly*.

From time $t = t_n$ to $t = t_{n+1}$, we combine the splitting steps via the fourth-order split-step method[25,45,11] and obtain a fourth-order time-splitting sine pseudospectral (**TSSP4**) method for the GPE (4.1). The detailed method is given by

$$\psi_j^{(1)} = e^{-i2w_1k(V_1(x_j)+\beta_1|\psi_j^n|^2)}\psi_j^n, \quad \psi_j^{(2)} = \sum_{l=1}^{M-1} e^{-iw_2k\mu_l^2}\,\hat{\psi}_l^{(1)}\sin(\mu_l(x_j-a)),$$

$$\psi_j^{(3)} = e^{-i2w_3k(V_1(x_j)+\beta_1|\psi_j^{(2)}|^2)}\psi_j^{(2)}, \quad \psi_j^{(4)} = \sum_{l=1}^{M-1} e^{-iw_4k\mu_l^2}\,\hat{\psi}_l^{(3)}\sin(\mu_l(x_j-a)),$$

$$\psi_j^{(5)} = e^{-i2w_3k(V_1(x_j)+\beta_1|\psi_j^{(4)}|^2)}\psi_j^{(4)}, \quad \psi_j^{(6)} = \sum_{l=1}^{M-1} e^{-iw_2k\mu_l^2}\,\hat{\psi}_l^{(5)}\sin(\mu_l(x_j-a)),$$

$$\psi_j^{n+1} = e^{-i2w_1k(V_1(x_j)+\beta_1|\psi_j^{(6)}|^2)}\psi_j^{(6)}, \quad j = 1,2,\ldots,M-1, \tag{4.10}$$

where $\hat{U}_l$, the sine-transform coefficients of a complex vector $U = (U_0, U_1, \ldots, U_M)$ with $U_0 = U_M = 0$, are defined as

$$\mu_l = \frac{\pi l}{b-a}, \quad \hat{U}_l = \frac{2}{M}\sum_{j=1}^{M-1} U_j\,\sin(\mu_l(x_j-a)), \quad l = 1,2,\ldots,M-1, \tag{4.11}$$

and[25,11]

$$w_1 = 0.33780\,17979\,89914\,40851, \quad w_2 = 0.67560\,35959\,79828\,81702,$$
$$w_3 = -0.08780\,17979\,89914\,40851, \quad w_4 = -0.85120\,71979\,59657\,63405.$$

The initial condition (4.2) is discretized as

$$\psi_j^0 = \psi(x_j,0) = \psi_0(x_j), \quad j = 0,1,2,\ldots,M. \tag{4.12}$$

Note that the only time discretization error of TSSP4 is the splitting error, which is fourth order in k for any fixed mesh size $h > 0$.

This scheme is explicit, time reversible, just as the IVP for the GPE. Also, a main advantage of the time-splitting method is its time-transverse invariance, just as it holds for the GPE itself. If a constant α is added to the potential V_1, then the discrete wave functions ψ_j^{n+1} obtained from TSSP4 are multiplied by the phase factor $e^{-i\alpha(n+1)k}$, which leaves the discrete quadratic observables unchanged. This property does not hold for finite difference schemes.

4.2. *Second-order TSSP for GPE with external driven field*

When $W(x,t) \neq 0$, i.e. with an external driven field, the GPE (4.1) can be rewritten in (4.5) with

$$A\psi = -\frac{1}{2}\partial_{xx}\psi(x,t), \quad B\psi = V_1(x)\psi(x,t) + W(x,t)\psi(x,t) + \beta_1|\psi(x,t)|^2\psi(x,t). \tag{4.13}$$

As the external driven field could be very complicated, e.g. it may be a Delta-function,[31] here we only use a second-order split-step scheme in time

discretization.[44] More precisely, from time $t = t_n$ to $t = t_{n+1}$, we proceed as follows:

$$\begin{aligned}
\psi_j^* &= \sum_{l=1}^{M-1} e^{-ik\mu_l^2/4}\, \widehat{(\psi^n)}_l\, \sin(\mu_l(x_j - a)),\\
\psi_j^{**} &= \exp\left[-ik(V_1(x_j) + \beta_1|\psi_j^n|^2) - i\int_{t_n}^{t_{n+1}} W(x_j,t)dt\right]\psi_j^*, \qquad (4.14)\\
\psi_j^{n+1} &= \sum_{l=1}^{M-1} e^{-ik\mu_l^2/4}\, \widehat{(\psi^{**})}_l\, \sin(\mu_l(x_j - a)), \quad j = 1,2,\ldots,M-1.
\end{aligned}$$

Remark 4.1. If the integral in (4.15) could not be evaluated analytically, one can use numerical quadrature to evaluate, e.g.

$$\int_{t_n}^{t_{n+1}} W(x_j,t)dt \approx \frac{k}{6}\left[W(x_j,t_n) + 4W(x_j,t_n + k/2) + W(x_j,t_{n+1})\right].$$

4.3. *Stability*

Let $U = (U_0, U_1, \ldots, U_M)^T$ with $U_0 = U_M = \mathbf{0}$ and let $\|\cdot\|_{l^2}$ be the usual discrete l^2-norm respectively on the interval (a,b), i.e.

$$\|U\|_{l^2} = \sqrt{\frac{b-a}{M}\sum_{j=1}^{M-1}|U_j|^2}. \qquad (4.15)$$

For the *stability* of the time-splitting spectral approximations TSSP4 (4.10) and second-order scheme (4.15), we have the following lemma, which shows that the total charge is conserved.

Lemma 4.1. *The fourth-order time-splitting sine pseudospectral scheme (TSSP4)* (4.10) *and second-order scheme* (4.15) *are unconditionally stable. In fact, for every mesh size $h > 0$ and time step $k > 0$,*

$$\|\psi^n\|_{l^2} = \|\psi^0\|_{l^2} = \|\psi_0\|_{l^2}, \quad n = 1,2,\ldots. \qquad (4.16)$$

Proof. Follows the line of the analogous result for the linear Schrödinger by time-splitting Fourier spectral approximation in Refs. 5, 8 and 9. □

5. Numerical Results

5.1. *Numerical accuracy*

In this subsection we present numerical results to confirm the spectral accuracy in space and fourth order accuracy in time for the numerical method (4.10). Comparison with the second-order time-splitting Fourier pseudospectral (TSFP2) method[6] for GPE is also reported.

Example 5.1. 1D Gross–Pitaevskii equation, i.e. in (1.4) we choose $d = 1$ and $\gamma_x = 1$. The initial condition is taken as

$$\psi_0(x) = \frac{1}{\pi^{1/4}} e^{-x^2/2}, \quad x \in \mathbb{R}.$$

We solve on the interval $[-32, 32]$, i.e. $a = -32$ and $b = 32$ with homogeneous Dirichlet boundary condition (4.2). We compute a numerical solution by using TSSP4 with a very fine mesh, e.g. $h = \frac{1}{128}$, and a very small time step, e.g. $k = 0.0001$, as the "exact" solution ψ. Let $\psi^{h,k}$ denote the numerical solution under mesh size h and time step k.

First we test the spectral accuracy of TSSP4 in space. In order to do so, for each fixed β_1, we solve the problem with different mesh size h but a very small time step, e.g. $k = 0.0001$, such that the truncation error from time discretization is negligible comparing to that from space discretization. Table 1 shows the errors $\|\psi(t) - \psi^{h,k}(t)\|_{l^2}$ at $t = 2.0$ with $k = 0.0001$ for different β_1 and h.

Then we test the fourth-order accuracy of TSSP4 in time. In order to do so, for each fixed β_1, we solve the problem with different time step k but a very fine mesh, e.g. $h = \frac{1}{64}$, such that the truncation error from space discretization is negligible comparing to that from time discretization. Table 2 shows the errors $\|\psi(t) - \psi^{h,k}(t)\|_{l^2}$ at $t = 2.0$ with $h = \frac{1}{64}$ for different β_1 and k.

For comparison, Tables 3 and 4 shows similar numerical results of TSFP2[6] for this example as in Tables 1 and 2.

From Tables 1–2 and 3–4, we can draw the following conclusions: (i) spectral order accuracy for spatial derivatives and fourth-order accuracy for time derivative of TSSP4 are demonstrated numerically for 1D GPE, respectively; (ii) for fixed β_1 and mesh size h, when time step k sufficiently small, the accuracy of TSSP4 and TSFP2 are the same; (iii) for fixed β_1 and time step k, TSSP4 is much more accurate than TSFP2. In fact, when $\beta_1 = 10$, TSSP4 needs $k = \frac{1}{640}$ to achieve

Table 1. Spatial error analysis for TSSP4: Error $\|\psi(t) - \psi^{h,k}(t)\|_{l^2}$ at $t = 2.0$ with $k = 0.0001$ in Example 5.1.

Mesh	$h = 1$	$h = \frac{1}{2}$	$h = \frac{1}{4}$	$h = \frac{1}{8}$	$h = \frac{1}{16}$
$\beta_1 = 10$	0.2745	1.081E-2	1.805E-6	3.461E-11	
$\beta_1 = 20\sqrt{2}$	1.495	0.1657	7.379E-4	7.588E-10	
$\beta_1 = 80$	1.603	1.637	6.836E-2	3.184E-5	3.47E-11

Table 2. Temporal error analysis for TSSP4: $\|\psi(t) - \psi^{h,k}(t)\|_{l^2}$ at $t = 2.0$ with $h = \frac{1}{64}$ in Example 5.1.

Time step	$k = \frac{1}{20}$	$k = \frac{1}{40}$	$k = \frac{1}{80}$	$k = \frac{1}{160}$	$k = \frac{1}{320}$	$k = \frac{1}{640}$
$\beta_1 = 10.0$	1.261E-4	8.834E-6	5.712E-7	3.602E-8	2.254E-9	1.422E-10
$\beta_1 = 20\sqrt{2}$	1.426E-3	9.715E-5	6.367E-6	4.034E-7	2.529E-8	1.580E-9
$\beta_1 = 80$	4.375E-2	1.693E-3	8.982E-5	5.852E-6	3.706E-7	2.323E-8

Table 3. Spatial error analysis for TSFP2: Error $\|\psi(t) - \psi^{h,k}(t)\|_{l^2}$ at $t = 2.0$ with $k = 0.0001$ in Example 5.1.

Mesh	$h = 1$	$h = \frac{1}{2}$	$h = \frac{1}{4}$	$h = \frac{1}{8}$	$h = \frac{1}{16}$
$\beta_1 = 10$	0.2719	1.077E-2	1.803E-6	1.008E-12	
$\beta_1 = 20\sqrt{2}$	1.484	0.1647	7.377E-4	7.588E-10	
$\beta_1 = 80$	1.602	1.657	6.807E-2	3.184E-5	1.702E-12

Table 4. Temporal error analysis for TSFP2: $\|\psi(t) - \psi^{h,k}(t)\|_{l^2}$ at $t = 2.0$ with $h = \frac{1}{64}$ in Example 5.1.

Time step	$k = \frac{1}{20}$	$k = \frac{1}{40}$	$k = \frac{1}{80}$	$k = \frac{1}{160}$	$k = \frac{1}{320}$	$k = \frac{1}{640}$
$\beta_1 = 10.0$	9.173E-4	2.285E-4	5.708E-5	1.426E-5	3.563E-6	8.880E-7
$\beta_1 = 20\sqrt{2}$	4.020E-3	9.945E-4	2.481E-4	6.198E-5	1.548E-5	3.858E-6
$\beta_1 = 80$	2.771E-2	4.768E-3	1.178E-3	2.941E-4	7.343E-5	1.830E-5

the accuracy 10^{-10}, but TSFP2 needs about $k = \frac{1}{640\times 80}$ in order to achieve the same accuracy. This implies that the time step of TSFP2 is 80 times less than that of TSSP4 in order to achieve very high accuracy. Thus the computational time of TSSP4 may be 25 times less than that of TSFP2.

Another issue is how to choose mesh size h and time step k in the strong repulsive interaction regime or semiclassical regime, i.e. $\beta_d \gg 1$, in order to get "correct" physical observables. In fact, after a rescaling in (1.4) under the normalization (1.7): $\mathbf{x} \to \varepsilon^{-1/2}\mathbf{x}$ and $\psi \to \varepsilon^{d/4}\psi$ with $\varepsilon = \beta_d^{-2/(d+2)}$, the GPE (1.4) can be rewritten as

$$i\varepsilon\, \partial_t \psi(\mathbf{x}, t) = -\frac{\varepsilon^2}{2}\nabla^2\psi + V_d(\mathbf{x})\psi + |\psi|^2\psi, \quad \mathbf{x} \in \mathbb{R}^d. \tag{5.1}$$

Similar as demonstrated in Refs. 8 and 9, the meshing strategy of TSSP4 to capture "correct" physical observables for this problem is

$$h = O(\varepsilon), \quad k = O(\varepsilon).$$

Thus the admissible meshing strategy of TSSP4 for GPE with strong repulsive interaction is

$$h = O(\varepsilon) = O\left(1/\beta_d^{2/(d+2)}\right), \quad k = O(\varepsilon) = O\left(1/\beta_d^{2/(d+2)}\right), \quad d = 1, 2, 3. \tag{5.2}$$

5.2. *Dynamics of the ground state*

In this subsection we apply TSSP4 to study the dynamics of the ground state and condensate width. Here the initial data is always chosen as the ground state. This setup is different from a similar study [6] in which the initial data was chosen as either the harmonic oscillator approximation or TF approximation. Furthermore, here we study the dynamics in 1D, 2D and 3D cases. This is also different from the results reported in the physical literatures for only 1D and 2D by different numerical methods.[16,18,19,23,43]

Example 5.2. 1D Gross–Pitaevskii equation, i.e. in (1.4) we choose $d = 1$. The initial condition is taken as the ground-state solution of (1.4) with $d = 1$, $\gamma_x = 1$ and $\beta_1 = 20.0$,[4,12] i.e. initially the condensate is assumed to be in its ground state. At $t = 0$, we double the trap frequency by setting $\gamma_x = 2$.

We solve this problem on the interval $[-12, 12]$ under mesh size $h = \frac{3}{64}$ and time step $k = 0.005$ with homogeneous Dirichlet boundary condition. Figure 1 plots the condensate width and central density $|\psi(0,t)|^2$ as functions of time, as well as evolution of the density $|\psi|^2$ in spacetime. One can see from this figure that the sudden change in the trap potential leads to oscillations in the condensate width and the peak value of the wave function. Note that the condensate width contracts in an oscillatory way (cf. Fig. 1(a)), which agrees with the analytical results in (3.13).

Example 5.3. 2D Gross–Pitaevskii equation, i.e. in (1.4) we choose $d = 2$. The initial condition is taken as the ground-state solution of (1.4) under $d = 2$ with $\gamma_x = 1$, $\gamma_y = 2$ and $\beta_2 = 20.0$,[4,12] i.e. initially the condensate is assumed to be in its ground state. At $t = 0$, we double the trap frequency by setting $\gamma_x = 2$ and $\gamma_y = 4$.

We solve this problem on $[-8, 8]^2$ under mesh size $h = \frac{1}{32}$ and time step $k = 0.005$ with homogeneous Dirichlet boundary condition. Figure 2 shows the condensate widths σ_x and σ_y as functions of time and the surface of the density $|\psi|^2$ at time $t = 5.4$, and Fig. 3 shows the contour plots of the density $|\psi|^2$ at different times. Again, the sudden change in the trap potential leads to oscillations in the condensate width. Due to $\gamma_y = 2\gamma_x$, the oscillation frequency of σ_y is roughly double that of σ_x and the amplitudes of σ_x are larger than those of σ_y in general (cf. Fig. 2(a)). Again this agrees with the analytical results in (3.13).

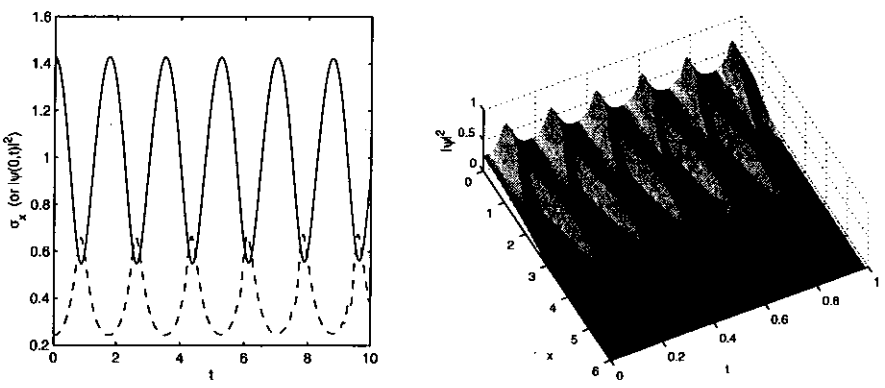

(a) (b)

Fig. 1. Numerical results for Example 5.2: (a) condensate width σ_x (solid line) and central density $|\psi(0,t)|^2$ (dashed line). (b) evolution of the density function $|\psi|^2$.

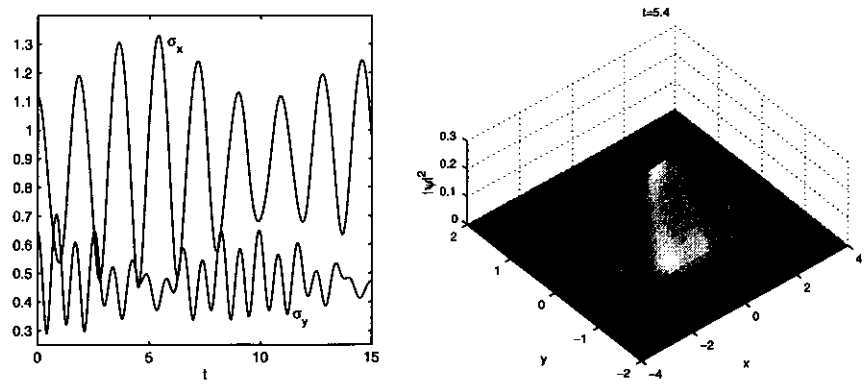

(a) (b)

Fig. 2. Numerical results for Example 5.3: (a) condensate width. (b) surface plot of the density $|\psi|^2$ at $t = 5.4$.

Example 5.4. 3D Gross–Pitaevskii equation, i.e. in (1.4) we choose $d = 3$. We present computations for two cases:

Case I. *Intermediate ratio between trap frequencies along different axis* (data for ^{87}Rb used in JILA[2]). The initial condition is taken as the ground-state solution of (1.4) under $d = 3$ with $\gamma_x = \gamma_y = 1$, $\gamma_z = 4$ and $\beta_3 = 37.62$.[4,12] At $t = 0$, we multiply the trap frequency four times by setting $\gamma_x = \gamma_y = 4$ and $\gamma_z = 16$.

Case II. *High ratio between trap frequencies along different axis* (data for ^{23}Na used in MIT (group of Ketterle)[21]). The initial condition is taken as the ground-state solution of (1.4) under $d = 3$ with $\gamma_x = \gamma_y = \frac{360}{3.5}$, $\gamma_z = 1$ and $\beta_3 = 3.083$.[4,12] At $t = 0$, we double the trap frequency by setting $\gamma_x = \gamma_y = \frac{720}{3.5}$ and $\gamma_z = 2$.

For case I, we solve the problem on $[-6,6]\times[-6,6]\times[-3,3]$ with mesh size $h_x = h_y = \frac{3}{32}$ and $h_z = \frac{3}{64}$, and time step $k = 0.0025$, and for case II, on $[-0.5,0.5] \times [-0.5,0.5] \times [-8,8]$ with $h_x = h_y = \frac{1}{128}$, $h_z = \frac{1}{8}$, and $k = 0.0005$. Homogeneous Dirichlet boundary conditions are used for the two cases.

Figure 4 shows the condensate widths $\sigma_x = \sigma_y$ and σ_z as functions of time, as well as the surface of the density in xz-plane $|\psi(x,0,z,t)|^2$. Similar phenomena in case I in 3D is observed as those in Example 5.3 which is in 2D (cf. Fig. 4(a)). The ratio between the condensate widths increases with increasing ratio between trap frequencies along different axis, i.e. it becomes more difficult to excite oscillations for large trap frequencies. In case II, the curves of the condensate widths are very well separated. This behavior is one of the basic assumptions allowing the reduction of GPE to 2D and 1D in the cases of one or two of the trap frequencies are much larger than the others.[33,12,6]

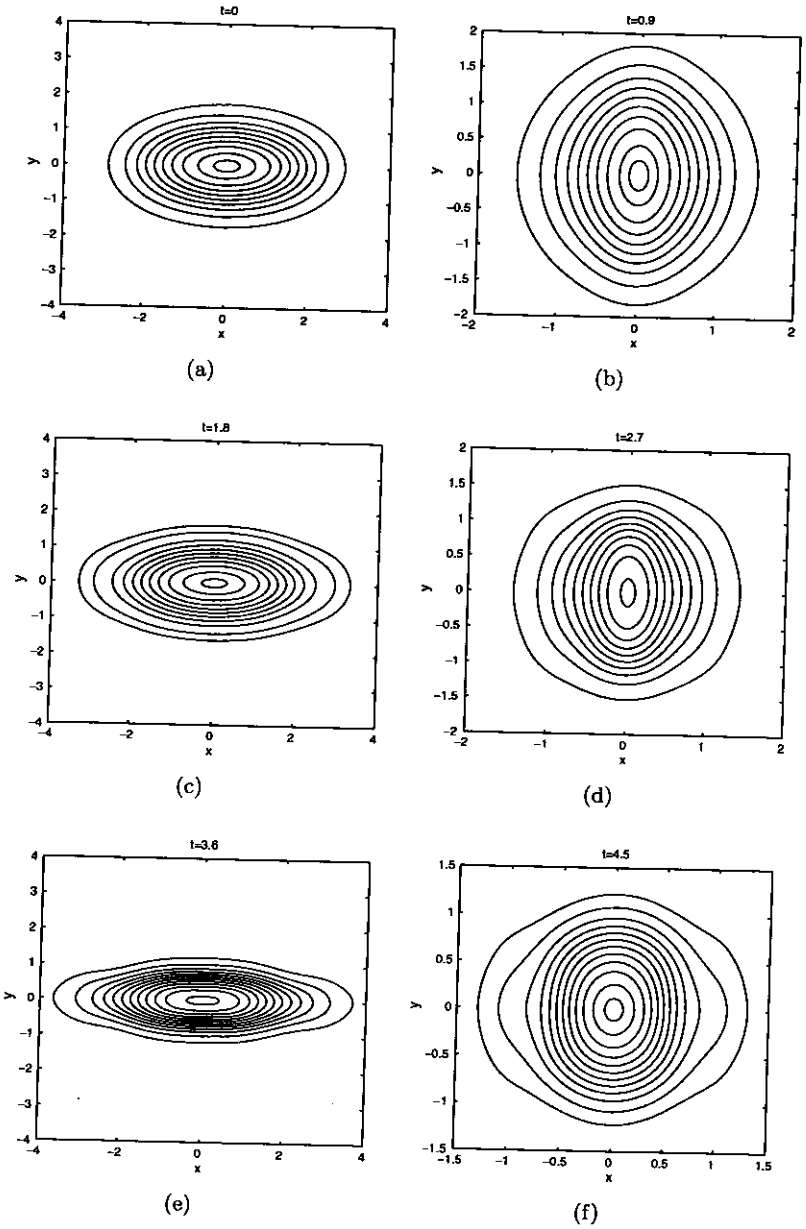

Fig. 3. Contour plots of the density $|\psi|^2$ at different times in Example 5.3. (a) $t = 0$, (b) $t = 0.9$, (c) $t = 1.8$, (d) $t = 2.7$, (e) $t = 3.6$, (f) $t = 4.5$.

5.3. *Stability of central vortex states*

In this subsection we study numerically the stability of central vortex states. Notice that similar study was also carried out in the physical literatures[15,29,30] by a different numerical method, where their method had difficulty in strong repulsive interaction regime.[15]

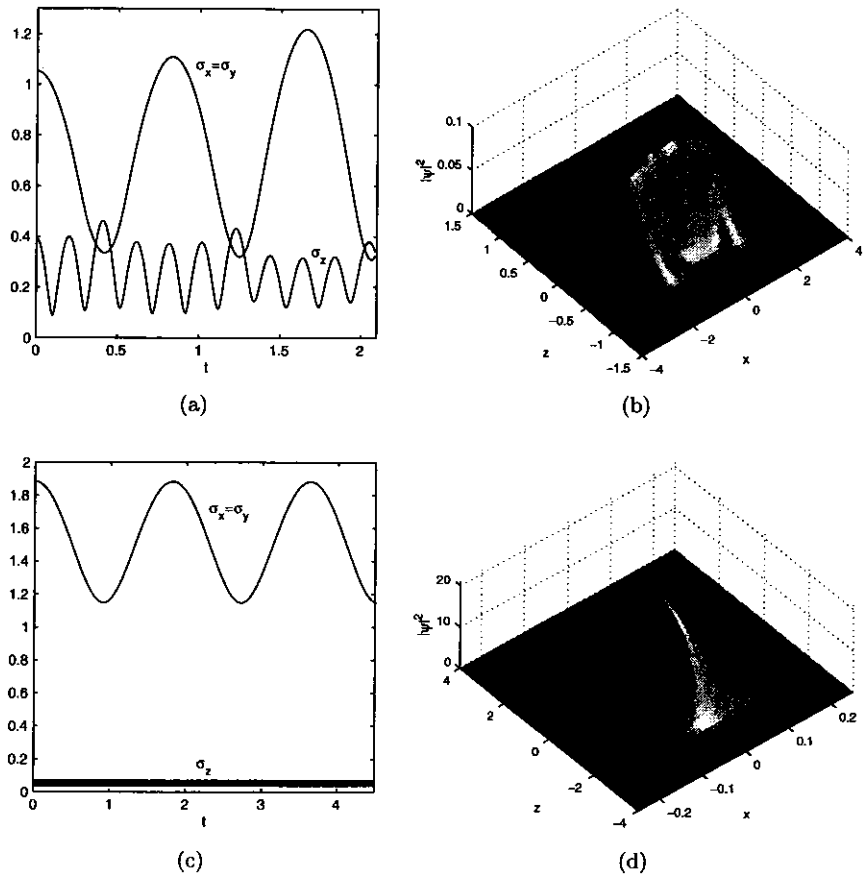

Fig. 4. Numerical results for Example 5.4: Left column: Condensate width; right column: Surface plot of the density in xz-plane, $|\psi(x,0,z,t)|^2$. Case I: (a) and (b) at $t = 1.64$. Case II: (c) and (d) at $t = 4.5$.

We choose $d = 2$, $\beta_2 = 100$ and $\gamma_x = \gamma_y = 1$ in (1.4). The initial data is chosen as the central vortex state with setting $W \equiv 0$. Then we perturb the condensate by inserting a Gaussian stirrer (given by Eq. (4.3) with $w_s = 1$) at a fixed position $x_s(t) \equiv x_s = 3$ and $y_s(t) \equiv y_s = 0$, with a stirrer height given by $W_s(t) = W_0 \sin^2 2t$ between $t = 0$ and $t = \pi/2$ with $W_0 = 10$. After $t = \pi/2$, the perturber is removed. The stability is studied by solving the 2D GPE with an external driven field (4.3) by the numerical method (4.15). To quantify the numerical results, we define the hydrodynamic velocity

$$\mathbf{u} = (u, v) = \mathrm{Im}(\psi^* \nabla\psi)/|\psi|^2.$$

Figure 5 shows the velocity field for dynamics of central vortex states with winding numbers 1 and 2. Furthermore, Fig. 6 plots the time evolution of the energy and angular momentum expectation for $m = 1, 2$.

From Fig. 5 and additional numerical simulation, we find that the central vortex states with index (or winding number) $m = \pm 1$ are dynamically stable, and

respectively, unstable when $|m| > 1$. These results confirm the numerical results in Ref. 15 by fourth-order Runge–Kutta spectral method, which is not time reversible and time transverse invariant, for GPE. Due to the limitation of that method, the authors could not do this study in the strong repulsive interaction regime.[15] Due to the "good" properties of our numerical method, we do not have that difficulty. Furthermore, Fig. 6 shows the energy increases and angular momentum expectation decreases when $t \in [0, \pi/2]$ due to the appearance of the perturber. After remove the perturber at $t = \pi/2$, they are conserved with time, which confirm the conservation laws (1.8) and (3.25).

5.4. *Interaction of central vortex states*

In this subsection we study the interaction between a few central vortices with index $m = \pm 1$. To our knowledge, no similar numerical study and results was reported in the physical literatures.

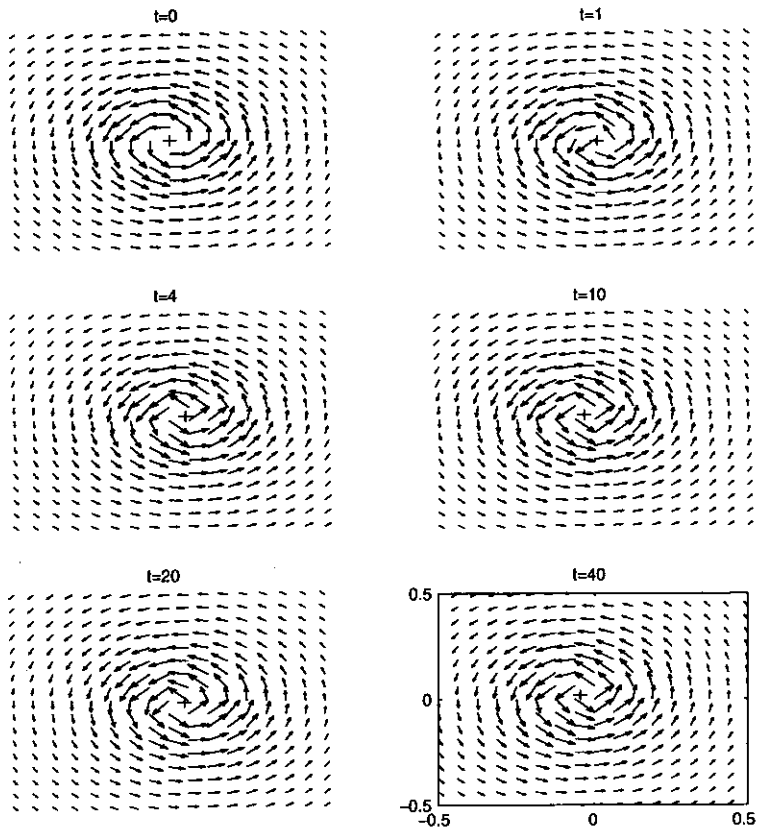

(a)

Fig. 5. Velocity field at different times for dynamics of central vortex states in Sec. 5.3. (a) $m = 1$, (b) $m = 2$.

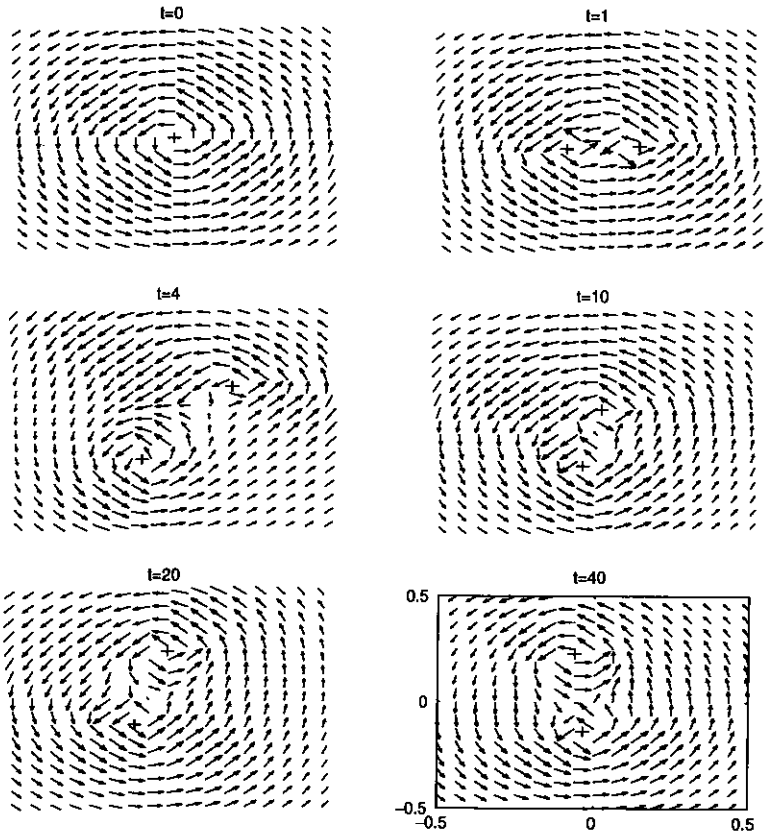

(b)

Fig. 5. (*Continued*)

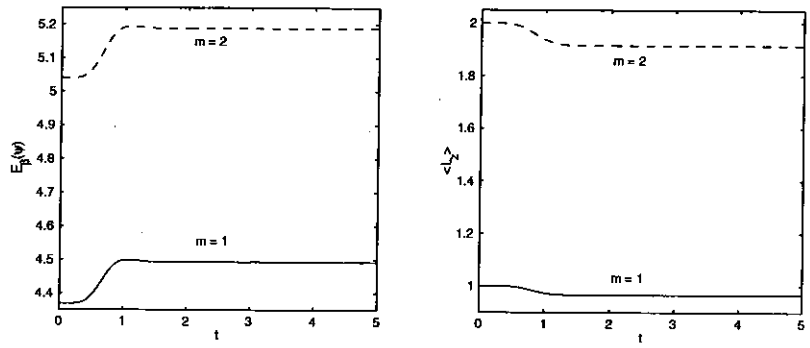

(a) (b)

Fig. 6. (a) time evolution of the energy $E_\beta(\psi)$ and (b) angular momentum expectation $\langle L_z \rangle$ for $m = 1, 2$ in Sec. 5.3.

In order to do so, we choose $d = 2$, $\beta_2 = 100$ and $\gamma_x = \gamma_y = 1$ in (1.4). The initial data (1.5) is chosen as

$$\psi(\mathbf{x},0) = \psi_0(x,y) = \frac{\prod_{j=1}^{M} \phi_\beta^{m_j}(\mathbf{x}-\mathbf{x}_j^0)}{\|\prod_{j=1}^{M} \phi_\beta^{m_j}(\mathbf{x}-\mathbf{x}_j^0)\|} = \frac{\prod_{j=1}^{M} \phi_\beta^{m_j}(x-x_j^0, y-y_j^0)}{\|\prod_{j=1}^{M} \phi_\beta^{m_j}(x-x_j^0, y-y_j^0)\|}, \quad (5.3)$$

where M is the total number of vortices, $\phi_\beta^{m_j}$ is the central vortex state of (2.1) with index m_j ($m_j = 1$ or -1).

We study ten cases of interaction by solving the 2D GPE (1.4) with initial data (5.3) by the numerical method (4.10). The parameters for the ten cases are displayed in Table 5. Figure 7 displays the time-evolution of vortex centers for the ten cases.

In case I, we study the dynamics of one central vortex. In order to do so, we shift the center of a central vortex with winding number $m = 1$ from the trap center, i.e. the origin $(0,0)$, to $\mathbf{x}_1^0$. This corresponds to shifting the trap center from origin to $-\mathbf{x}_1^0$. The dynamics of the vortex center is (cf. Fig. 7(a)):

$$\mathbf{x}_1(t) = \mathbf{x}_1^0 \cos t, \quad t \geq 0.$$

This implies that the dynamics of vortex center satisfies the following ODE:

$$\ddot{\mathbf{x}}_1(t) + \mathbf{x}_1(t) = 0, \quad t > 0, \quad \mathbf{x}_1(0) = \mathbf{x}_1^0, \quad \dot{\mathbf{x}}_1(0) = \mathbf{0}. \quad (5.4)$$

From Fig. 7(a), we can see that the vortex center $(x_1(t), y_1(t))$ oscillates across the trap center in a periodic way with period $T = 2\pi$ and the distance between the vortex center and the trap center is a periodic function with period $T = \pi$ which is independent of the initial position of the central vortex, i.e. $\mathbf{x}_1^0$. A mathematical justification by constructing exact solution for the GPE in this case is given in Ref. 26. Our additional numerical experiments show similar results for one central vortex with index $m = -1$.

In cases II and III, we study the interaction between two central vortices with the same index, e.g. $m_1 = m_2 = 1$. In case II, the centers of the two vortices are initially symmetric to the trap center, where in III, they are not. From Figs. 7(b) and (c), we can draw the following conclusions: (i) The centers of the two vortices

Table 5. Setup for different interactions.

Case	M	$\mathbf{x}_1^0 = (x_1^0, y_1^0)$	m_1	$\mathbf{x}_2^0 = (x_2^0, y_2^0)$	m_2	$\mathbf{x}_3^0 = (x_3^0, y_3^0)$	m_3
I	1	(1,2)	1				
II	2	(1,0)	1	(−1,0)	1		
III	2	(1,0)	1	(0,0)	1		
IV	2	(1,0)	1	(−1,0)	−1		
V	2	(1.5,0)	1	(−1.5,0)	−1		
VI	2	(1,0)	1	(0,0)	−1		
VII	2	(3,0)	1	(0,0)	−1		
VIII	3	(1,0)	1	(−1,0)	1	(0,0)	1
IX	3	(1,0)	1	(−1,0)	1	(0.5,0.5)	1
X	3	(1,0)	1	(−1,0)	1	(−0.5,1)	−1

with the same index rotate symmetrically around the trap center in case II (cf. Fig. 7(b)), and respectively, nonsymmetrically in case III (cf. Fig. 7(c)), which implies that the symmetry/nonsymmetry between the two vortex centers at $t = 0$ is kept during the interaction; (ii) the two vortices do NOT collide at any time; (iii) the two vortex centers move in a quasi-periodic manner with a period $T \approx 4\pi$

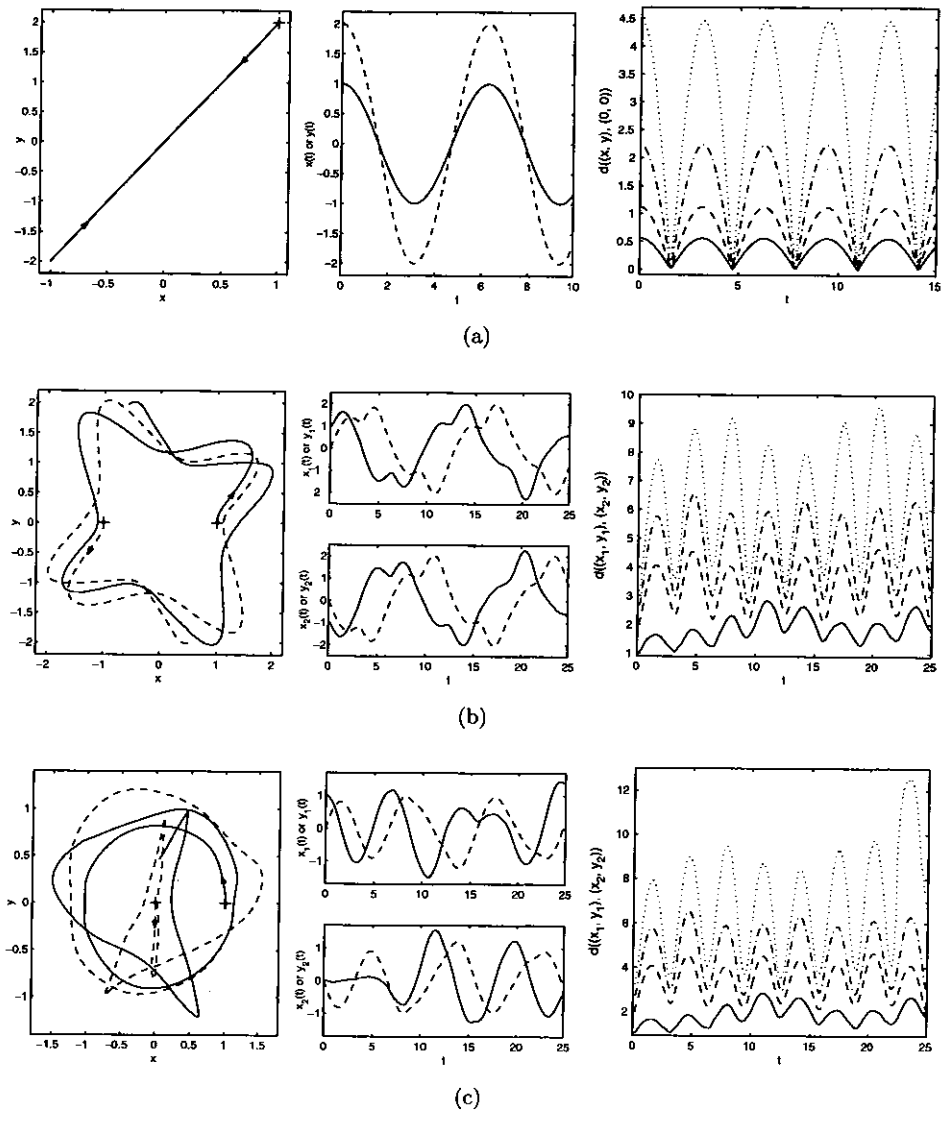

Fig. 7. Motion of vortex centers in Sec. 5.4. Left column: trajectory; middle column: motion with respect to time t, solid line for x and dashed line for y; left column: distance between vortex centers with respect to time t. '•': initial position of vortex centers, '+': index $m = 1$, '−': index $m = -1$, 'O': collision position of two vortices with opposite indices. (a) case I, (b) case II, (c) case III, (d) case IV, (e) case V, (f) case VI, (g) case VII, (h) case VIII, (i) case IX and (j) case X.

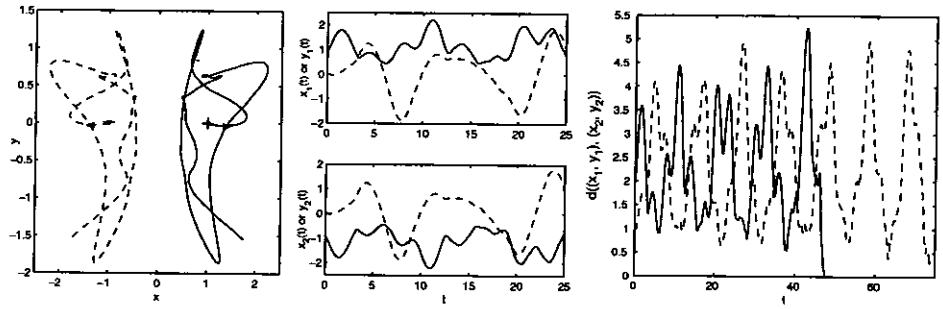

(d)

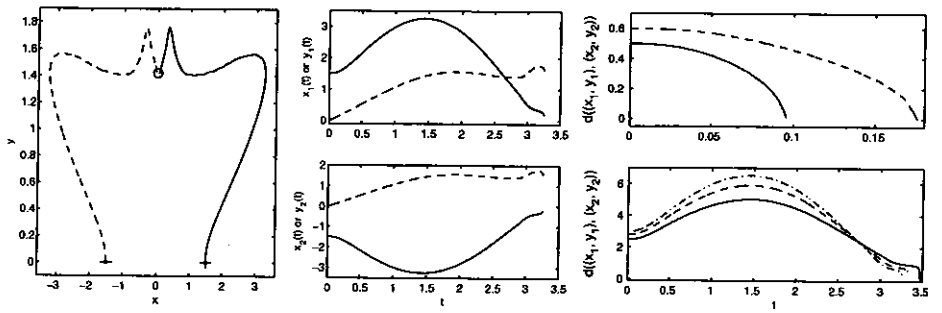

(e)

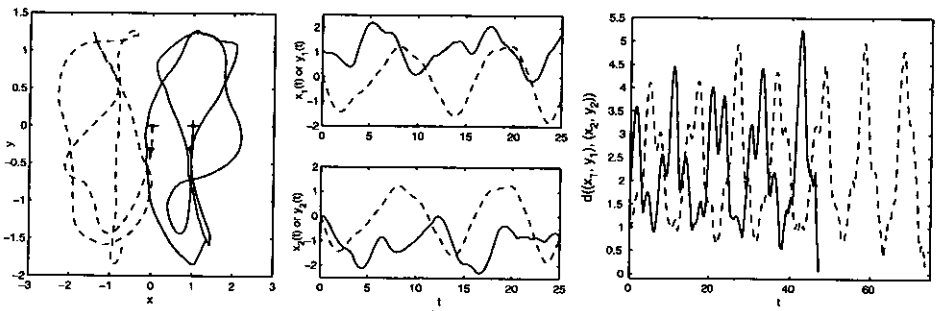

(f)

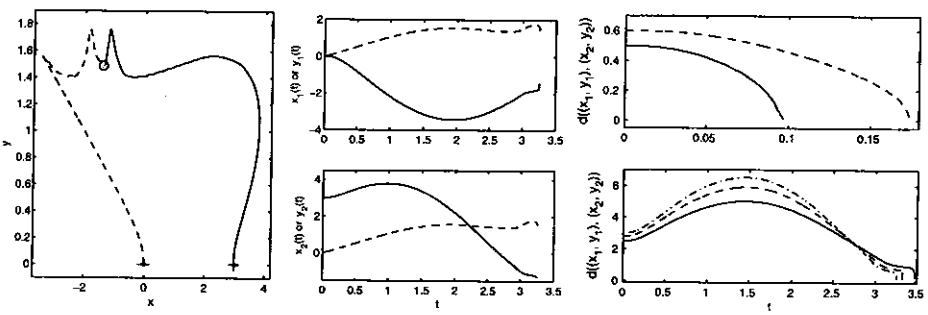

(g)

Fig. 7. (*Continued*)

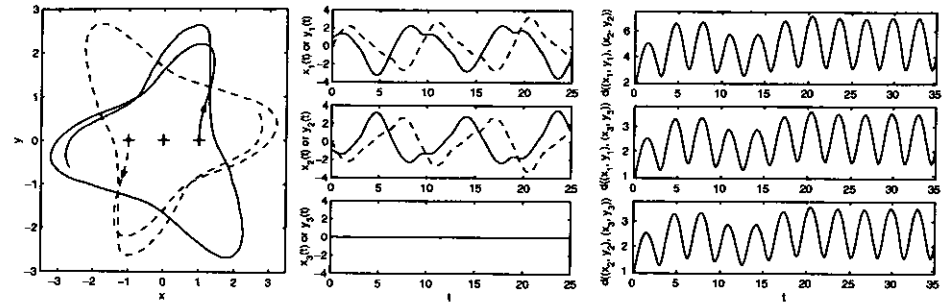

(h)

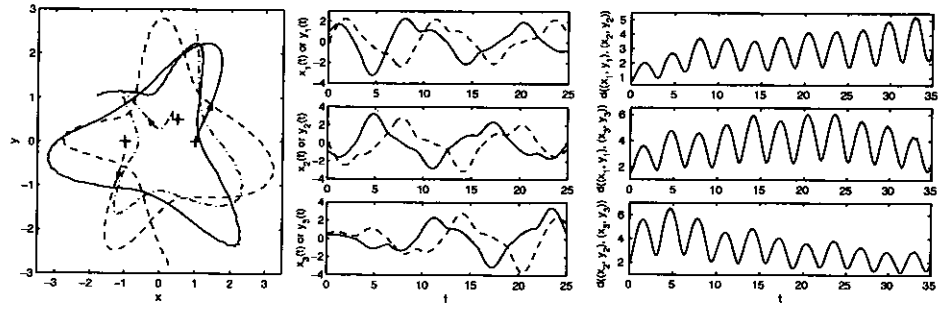

(i)

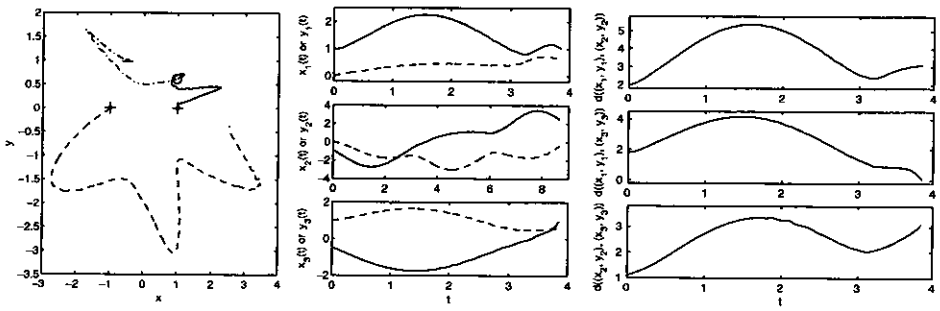

(j)

Fig. 7. (*Continued*)

and the distance between the two vortex centers is also a quasi-periodic function with period $T = \pi$, which is independent of the distance between the two vortices at $t = 0$ and their initial positions. Similar interaction patterns between two central vortices with index $m_1 = m_2 = -1$ are observed from our additional numerical experiments.

In cases IV, V, VI and VII, we study the interaction between two central vortices with different indices, e.g. $m_1 = 1$ and $m_2 = -1$. In cases IV and V, the centers of the two vortices are initially symmetric to the trap center, in VI and VII, they are

not. In cases IV and VI, the distance between the two vortices at $t = 0$ is between 1 to 2, which is about one to two times the core size ($R_c \approx 1.11$ for $\beta = 100$, cf. Fig. 6 in Ref. 4) of a central vortex with $m = 1$; in cases V and VII, it is either much less or much bigger than the core size. From Figs. 7(d)–(g), we can draw the following conclusions: (i) The two vortex centers move symmetrically to the trap center in cases IV and V, and respectively, nonsymmetrically in cases VI and VII, which again implies that the symmetry/nonsymmetry between the two vortex centers at $t = 0$ is kept during the interaction; (ii) the two vortices with opposite index will always collide after some time and then disappear together; (iii) the collision time depends on the initial distance between the two vortex centers and is almost independent of the initial positions of the two vortices, the collision time will increase (decrease) when the initial distance between the two vortices increases and is less (bigger) than the core size of a central vortex, and usually when the initial distance is equal to the core size of a central vortex, the collision time attains its maximum; (iv) when the initial distance between the two vortex centers is around one to two times, the core size of a central vortex, the two centers oscillate separately and their distance also oscillates with time and eventually goes to zero; (v) when the initial distance between the two vortex centers is much less or bigger than the core size of a central vortex, the two centers almost go directly to the collision point; (vi) if the centers of the two vortices are initially symmetric to the trap center, the collision point is always on the line perpendicular to the line defined by the two initial vortex centers. In fact, in Tables 6 and 7, we list collision times and coordinates of collision points with different initial distances and positions.

In cases VIII and IX, we study the interaction between three central vortices with the same index, e.g. $m_1 = m_2 = m_3 = 1$. In case VIII, one vortex is initially put at the trap center and the other two are positioned symmetric to the trap center; in case IX, the three vortices are put nonsymmetrically. From Figs. 7(h) and (i), we can draw the following conclusions: (i) in case VIII the vortex initially at the trap center does not move at all and the other two vortex centers rotate symmetrically around the trap center, in case IX, nonsymmetric motion of the vortex centers

Table 6. Collision time and point of the interaction between two opposite central vortices, which are initially symmetric to the trap center, with different initial distance.

$\mathbf{x}_1^0$	$\mathbf{x}_2^0$	Distance d_0	Collision time T_{coll}	Collision point $\mathbf{x}_{\text{coll}}$
(−0.25,0)	(0.25,0)	0.5	0.094	(0,−0.28)
(−0.3,0)	(0.3,0)	0.6	0.173	(0,−0.39)
(−0.4,0)	(0.4,0)	0.8	9.02	(0,1.2)
(−0.5,0)	(0.5,0)	1.0	73.62	(0,−0.16)
(−1,0)	(1,0)	2	47.11	(0,0.41)
(−1.25,0)	(1.25,0)	2.5	3.47	(0,1.32)
(−1.4,0)	(1.4,0)	2.8	3.321	(0,1.58)
(−1.5,0)	(1.5,0)	3	3.2544	(0,1.549)

Table 7. Collision time and point of interaction between two opposite central vortices, which are initially not symmetric to the trap center, with different initial distance.

$\mathbf{x}_1^0$	$\mathbf{x}_2^0$	Distance d_0	Collision time T_{coll}	Collision point $\mathbf{x}_{\text{coll}}$
(0,0)	(0.5,0)	0.5	0.094	(0.245,−0.28)
(0,0)	(0.6,0)	0.6	0.174	(0.29,−0.39)
(0,0)	(0.8,0)	0.8	9.13	(−0.38,1.054)
(0,0)	(1,0)	1.0	73.63	(−0.1,−0.165)
(0,0)	(2,0)	2	47.12	(−0.99,0.41)
(0,0)	(2.5,0)	2.5	3.47	(−1.13,1.32)
(0,0)	(2.8,0)	2.8	3.32	(−1.11,1.53)
(0,0)	(3,0)	3	3.255	(−1.35,1.5)

is observed, again this implies that the symmetry/nonsymmetry between the three vortex centers at $t = 0$ is kept during the interaction; (ii) the three vortices do NOT collide at any time; (iii) the three vortex centers move in a quasi-periodic manner with a period $T \approx 3\pi$ and the distance between any two vortex centers is also a quasi-periodic function with period $T \approx \pi$, which is independent of the distance between the two vortices at $t = 0$ and their initial positions. Similar interaction patterns between three central vortices with index $m_1 = m_2 = m_3 = -1$ are observed from our additional numerical experiments.

In case X, we study the interaction between three central vortices with different index, e.g. $m_1 = m_2 = 1$ and $m_3 = -1$. From Fig. 7(j) we can see that two vortices with opposite index, initially at (1,0) with index $m_1 = 1$ and at $(-0.2, 1)$ with index $m_3 = -1$, among the three will collide at the point $(0.98, 0.616)$ and both disappear time $t = 3.852$. After the collision, there is only one vortex which is initially at $(-1, 0)$ left in the dynamics. Similar interaction patterns between three central vortices with index $m_1 = 1$ and $m_2 = m_3 = -1$ are observed from our additional numerical experiments.

From the above numerical study, we can draw the following conclusions: (i) interaction patterns between several central vortices in BEC is very interesting and complicated; (ii) two central vortices with opposite index will collide and disappear after some time, and collision time and position depends on the initial distance between the two vortex centers as well as the core size of one central vortex; (iii) symmetry/nonsymmetry between the vortex centers at $t = 0$ is usually kept during the interaction; (iv) for interaction between vortices with the same indices, the distance between any two vortex centers is a quasi-periodic function with a period $T \approx \pi$ which is independent of the distance between the two vortices at $t = 0$ and their initial positions; (v) if initially there are N vortices with indices m_j $(= \pm 1)$, $j = 1, \ldots, N$, after some time, there are only $\sum_{j=1}^{N} m_j$ single vortices left and all the others collide and disappear. Of course, dynamical laws that govern the motion of vortex centers in interaction between several central vortices, may be an ODE system like (5.4), need further study.

5.5. *Critical angular frequency*

In this subsection we find numerically the critical angular frequency for single vortex cycling from the ground state under a far-blue detuned Gaussian laser stirrer[15] by using the numerical method (4.15). Similar numerical simulation has been done in Ref. 15 by a different numerical method, where their method has difficulty when β_d is large.[15]

In order to do so, we choose $d = 2$, $\gamma_x = \gamma_y = 1$ in (1.4). The initial data (1.5) is chosen as the ground state solution of (1.4). At time $t = 0$, we apply a Gaussian stirrer (given by Eq. (4.3)) rotating with the trap center as $x_s(t) = r_s \cos(\omega_f t)$ and $y_s(t) = r_s \sin(\omega_f t)$, with a stirrer height given by $W_s(t) = W_0 t/t_0$ when $0 \leq t \leq t_0$, and W_0 when $t > t_0$. Due to the stirrer, vortices may be generated from the initial ground state. A single vortex enters at the edge of the visible region of the condensate, then cycles to the center of the condensate, and back to the edge. This cycle repeats regularly.[15] This single vortex cycling occurs when the stirrer angular frequency ω_f is just below a critical angular frequency, which is denoted as ω_c.[15] The measure of appearance of single vortex cycling is done by computing the angular momentum expectation value $\langle L_z \rangle(t)$. It is very easy to see that $\langle L_z \rangle = 0$ for the ground state and $\langle L_z \rangle = 1$ for $m = 1$ central vortex state.

At lower stirring speeds ω_f, $\langle L_z \rangle$ remains much less than one (cf. Fig. 8). As ω_f increases, peak of $\langle L_z \rangle$ becomes larger until, for ω_f only slightly below ω_c, single vortex reaches the center of the condensate, and at its peak, $\langle L_z \rangle$ approaches one from below (cf. Fig. 8). If ω_f is increased above ω_c, multiple vortices penetrate the condensate and $\langle L_z \rangle$ exceeds one.

We find the critical angular frequency by solving the GPE with our method (4.15) for different β_2. In our simulation, we take $w_s = 2$, $r_s = 2$ and $W_0 = 10$ in (4.3). Table 8 displays the bounds for each value β_2: the lower bound is the

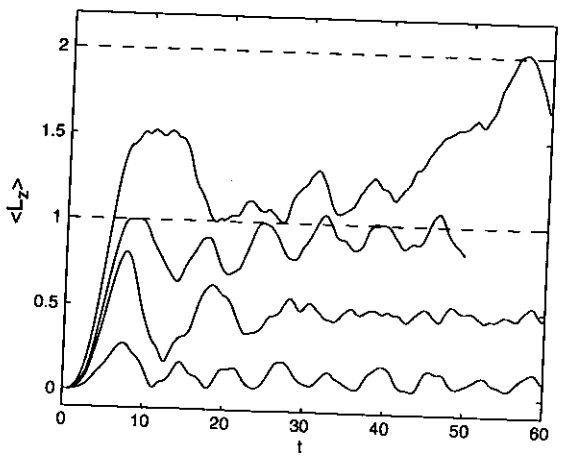

Fig. 8. Angular momentum expectation values versus time for $\beta_2 = 200$ with different $\omega_f = 0.45, 0.305, 0.25, 0.1$ (in the order of decreasing peak of $\langle L_z \rangle$).

Table 8. Critical angular frequency ω_c for 2D BEC.

β_2	E_β^g	E_β^1	$E_\beta^1 - E_\beta^g$	ω_c
25	2.1806	2.8091	0.6285	$0.55 \sim 0.65$
50	2.896	3.4167	0.5207	$0.42 \sim 0.55$
100	3.9459	4.3689	0.423	$0.35 \sim 0.5$
200	5.4624	5.8014	0.339	$0.30 \sim 0.42$
500	8.518	8.7606	0.2488	$0.21 \sim 0.32$

largest value of ω_f for which we have observed single vortex cycling, i.e. peak of $\langle L_z \rangle$ is near 1, where the upper bound is the smallest value of ω_f for which we found multiple vortex behavior, i.e. peak of $\langle L_z \rangle$ is near 2.

From Table 8, we find that the critical angular frequency ω_c decreases as the nonlinearity increases. When β_2 is not too large, our results agree with the results in Ref. 15 very well. Due to the high spatial/temporal resolution (5.2) of the method (4.15), our numerical method can be used to find ω_c in strong repulsive interaction regime.

6. Conclusions

Dynamics of the ground state and central vortex states in BEC is studied analytically and numerically. We prove that the ground state is a global minimizer of the energy functional over the unit sphere, and all excited states are saddle points, in linear GPE. Then we study time evolution of condensate width by deriving a second order ODE mathematically. We also study numerically stability of central vortex states, interaction of a few central vortices and critical angular frequency for single vortex cycling from the ground state by a fourth-order time-splitting sine-pseudospectral method. Our numerical results confirm the ODE for time evolution of condensate width, show that central vortices with winding number $m = \pm 1$ are dynamically stable, and respectively, unstable when $|m| > 1$. Furthermore, they also provide very interesting and complicated motion patterns between central vortex interactions. Numerical comparison with previous methods for GPE shows that the new method has better spatial/temporal resolution in strong repulsive interaction regime. Thus it could give better results for studying BEC in strong repulsive interaction regime or save computational time, especially in 3D.

Acknowledgments

The authors acknowledge support by the National University of Singapore grant No. R-151-000-030-112. W.B. thanks Qiang Du and Robert Pego for the helpful discussions. The authors thank the referees for their valuable comments and suggestions for improving the paper.

References

1. A. Aftalion and Q. Du, Vortices in a rotating Bose–Einstein condensate: Critical angular velocities and energy diagrams in the Thomas–Fermi regime, *Phys. Rev. A* **64** (2001) 063603.
2. M. H. Anderson, J. R. Ensher, M. R. Matthews, C. E. Wieman and E. A. Cornell, *Science* **269** (1995) 198.
3. W. Bao, Ground states and dynamics of multi-component Bose–Einstein condensates, *Multiscale Model. Simul.* **2** (2004) 210–236.
4. W. Bao and Q. Du, Computing the ground state solution of Bose–Einstein condensates by a normalized gradient flow, *SIAM J. Sci. Comput.* **25** (2004) 1674–1697.
5. W. Bao and D. Jaksch, An explicit unconditionally stable numerical methods for solving damped nonlinear Schrodinger equations with a focusing nonlinearity, *SIAM J. Numer. Anal.* **41** (2003) 1406–1426.
6. W. Bao, D. Jaksch and P. A. Markowich, Numerical solution of the Gross–Pitaevskii equation for Bose–Einstein condensation, *J. Comput. Phys.* **187** (2003) 318–342.
7. W. Bao, D. Jaksch and P. A. Markowich, Three dimensional simulation of jet formation in collapsing condensates, *J. Phys. B: At. Mol. Opt. Phys.* **37** (2004) 329–343.
8. W. Bao, S. Jin and P. A. Markowich, On time-splitting spectral approximations for the Schrödinger equation in the semiclassical regime, *J. Comput. Phys.* **175** (2002) 487–524.
9. W. Bao, S. Jin and P. A. Markowich, Numerical study of time-splitting spectral discretizations of nonlinear Schrödinger equations in the semi-clasical regimes, *SIAM J. Sci. Comput.* **25** (2003) 27–64.
10. W. Bao, L. Pareschi and P. A. Markowich, Quantum kinetic theory: Modelling and numerics for Bose–Einstein condensation, in *Modeling and Computational Methods for Kinetic Equations*, eds. P. Degond *et al.* (Birkhäuser, 2003), pp. 287–320.
11. W. Bao and J. Shen, A fourth-order time-splitting Laguerre-Hermite pseudo-spectral method for Bose–Einstein condensates, *SIAM J. Sci. Comput.* **26** (2005) 2010–2028.
12. W. Bao and W. Tang, Ground state solution of trapped interacting Bose–Einstein condensate by directly minimizing the energy functional, *J. Comput. Phys.* **187** (2003) 230–254.
13. G. Baym and C. J. Pethick, Ground-state properties of magnetically trapped Bose-condensed Rubidium gas, *Phys. Rev. Lett.* **76** (1996) 6–9.
14. C. C. Bradley, C. A. Sackett and R. G. Hulet, Bose–Einstein condensation of lithium: Observation of limited condensate number, *Phys. Rev. Lett.* **78** (1997) 985–989.
15. B. M. Caradoc-Davis, R. J. Ballagh, K. Burnett, Coherent dynamics of vortex formation in trapped Bose–Einstein condensates, *Phys. Rev. Lett.* **83** (1999) 895.
16. L. D. Carr, Charles W. Clark and W. P. Reinhardt, Stationary solutions of the one-dimensional nonlinear Schrodinger equation I. Case of repulsive nonlinearity, *Phys. Rev. A* **62** (2000) 063610.
17. S.-M. Chang, W.-W. Lin and S.-F. Shieh, Gauss–Seidel-type methods for energy states of a multi-component Bose–Einstein condensate, *J. Comput. Phys.* **202** (2005) 367–390.
18. M. M. Cerimele, M. L. Chiofalo, F. Pistella, S. Succi and M. P. Tosi, Numerical solution of the Gross–Pitaevskii equation using an explicit finite-difference scheme: An application to trapped Bose–Einstein condensates, *Phys. Rev. E* **62** (2000) 1382–1389.
19. M. L. Chiofalo, S. Succi and M. P. Tosi, Ground state of trapped interacting Bose–Einstein condensates by an explicit imaginary-time algorithm, *Phys. Rev. E* **62** (2000) 7438–7444.

20. F. Dalfovo, S. Giorgini, L. P. Pitaevskii and S. Stringari, Theory of Bose–Einstein condensation in trapped gases, *Rev. Mod. Phys.* **71** (1999) 463–512.
21. K. B. Davis, M. O. Mewes, M. R. Andrews, N. J. van Druten, D. S. Durfee, D. M. Kurn and W. Ketterle, *Phys. Rev. Lett.* **75** (1995) 3969.
22. M. Edwards, P. A. Ruprecht, K. Burnett, R. J. Dodd and C. W. Clark, *Phys. Rev. Lett.* **77** (1996) 1671; D. A. W. Hutchinson, E. Zaremba and A. Griffin, *ibid.* **78** (1997) 1842.
23. M. Edwards and K. Burnett, Numerical solution of the nonlinear Schrödinger equation for small samples of trapped neutral atoms, *Phys. Rev. A* **51** (1995) 1382.
24. D. L. Feder, A. A. Svidzinsky, A. L. Fetter and C. W. Clark, Anomalous modes drive vortex dynamics in confined Bose–Einstein condensates, *Phys. Rev. Lett.* **86** (2001) 564–567.
25. B. Fornberg and T. A. Driscoll, A fast spectral algorithm for nonlinear wave equations with linear dispersion, *J. Comput. Phys.* **155** (1999) 456.
26. J. J. Garcia-Ripoll, V. M. Perez-Garcia and V. Vekslerchik, Construction of exact solutions by spatial translations in inhomogeneous nonlinear Schrödinger equaitons, *Phys. Rev. E* **64** (2001) 056602.
27. E. P. Gross, Structure of a quantized vortex in boson systems, *Nuovo Cimento* **20** (1961) 454–477.
28. D. S. Hall, M. R. Mattthews, J. R. Ensher, C. E. Wieman and E. A. Cornell, Dynamics of component separation in a binary mixture of Bose–Einstein condensates, *Phys. Rev. Lett.* **81** (1998) 1539–1542.
29. B. Jackson, J. F. McCann and C. S. Adams, Vortex formation in dilute inhomogeneous Bose–Einstein condensates, *Phys. Rev. Lett.* **80** (1998) 3903–3906.
30. B. Jackson, J. F. McCann and C. S. Adams, Dissipation and vortex creation in Bose–Einstein condensated gases, *Phys. Rev. A* **61** (2000) 051603.
31. D. Jaksch, C. Bruder, J. I. Cirac, C. W. Gardiner and P. Zoller, Cold bosonic atoms in optical lattices, *Phys. Rev. Lett.* **81** (1998) 3108–3111.
32. L. Laudau and E. Lifschitz, *Quantum Mechanics: Non-relativistic Theory* (Pergamon Press, 1977).
33. P. Leboeuf and N. Pavloff, *Phys. Rev. A* **64** (2001) 033602; V. Dunjko, V. Lorent and M. Olshanii, *Phys. Rev. Lett.* **86** (2001) 5413.
34. E. H. Lieb, R. Seiringer and J. Yugvason, Bosons in a trap: A rigorous derivation of the Gross-Pitaevskii energy functional, *Phys. Rev. A* **61** (2000) 3602.
35. F. Lin and T. C. Lin, Vortices in two-dimensional Bose–Einstein condensates, in *Geometry and Nonlinear Partial Differential Equations* (Hangzhou, 2001) AMS/IP Stud. Adv. Math., Vol. 29 (Amer. Math. Soc., 2002), pp. 87–114.
36. C. Lobo, A. Sinatra and Y. Castin, Vortex lattice formation in Bose–Einstein condensates, *Phys. Rev. Lett.* **92** (2004) 020403.
37. E. Lundh, J. P. Martikainen and K. A. Suominen, Vortex nucleation in Bose–Einstein condensates in time-dependent traps, *Phys. Rev. A* **67** (2003) 063604.
38. A. S. Parkins and D. F. Walls, *Phys. Rep.* **303** (1998) 1.
39. C. J. Pethick and H. Smith, *Bose–Einstein Condensation in Dilute Gases* (Cambridge Univ. Press, 2002).
40. L. P. Pitaevskii, Vortex lines in a imperfect Bose gase, *Zh. Eksp. Teor. Fiz.* **40** (1961) 646–649 [*Sov. Phys. JETP* **13** (1961) 451–454].
41. L. P. Pitaevskii and S. Stringari, *Bose–Einstein Condensation* (Clarendon Press, 2003).

42. D. S. Rokhsar, *Phys. Rev. Lett.* **79** (1997) 2164; R. Dum, J. I. Cirac, M. Lewenstein and P. Zoller, *ibid.* **80** (1998) 2972; P. O. Fedichev and G. V. Shlyapnikov, *Phys. Rev. A* **60** (1999) R1779.
43. P. A. Ruprecht, M. J. Holland, K. Burnett and M. Edwards, Time-dependent solution of nonlinear Schrödinger equation for Bose-condensated trapped neutral atoms, *Phys. Rev. A* **51** (1995) 4704–4711.
44. G. Strang, On construction and comparison of difference schemes, *SIAM J. Numer. Anal.* **5** (1968) 506.
45. H. Yoshida, Construction of higher order symplectic integrators, *Phys. Lett. A* **150** (1990) 262–268.